

## CAAP Quarterly Report

[3/31/2025]

**Project Name:** *Multi-Compound Green Corrosion Inhibitor for Gas Pipeline: Synthesis, Optimization, and Evaluation*

**Contract Number:** 693JK32350004CAAP

**Prime University:** Arizona State University

**Prepared By:** *Dr. Yongming Liu (PI), Dr. Shuguang Deng (Co-PI), Dr. Tekle Fida (Co-PI), Sai Niranjana, Xuandong Lu, Adi Venkata Sandeep Yalamanchili, Mohammadjavad Kazemi, Essam Abdel Rahman, Qihang Xu, Saumya, Dimple Mehta, Kapil Chandra Akula*

**Reporting Period:** [1/2025 – 3/2025]

### **Project Activities for Reporting Period:**

#### Task 1. Design and Synthesis of Multi-compound Green Inhibitors

The team focused on modifying triglycerides (oils) into fatty acid methyl esters (FAMES) and evaluating their potential as corrosion inhibitors. By comparing the inhibition efficiencies of mixed fatty acids (from natural sources) with those of pure, individual fatty acids, we aim to gain insights into their relative performance. Additionally, the study seeks to understand the similarities and differences in the corrosion inhibition mechanisms between free fatty acids and surfactant-type inhibitors. The findings will help select the most promising candidates for further chemical modification and development as environmentally friendly corrosion inhibitors.

- Task 1.1: Quick screening of green inhibitors for gas pipeline protection
  - Modified triglycerides (oils) into fatty acid methyl esters (FAMES) for corrosion inhibition studies.
  - Compare the inhibitor efficiency of mixed fatty acids with pure fatty acids.
  - Investigated the differences and similarities in inhibition mechanisms between free fatty acids and surfactants.
  - Evaluated performance to identify effective candidates for further modification.
  - Aimed to develop eco-friendly and efficient corrosion inhibitors based on experimental results.
  - Natural product-based biocorrosion inhibitor screening (GTI effort)

## Task 2. Simulation-based Inhibitor Optimization in Gas Gathering and Transportation Pipelines

During this reporting period, we have made significant progress in Task 2, focusing on applying the AI-enhanced approach for more efficient prediction of the inhibitor deposition and further establishing a probabilistic model to evaluate the reliability of the protective film. The key activities are outlined below:

- 2.1: Numerical simulation of multiphase flow for inhibitor distribution in gas pipeline systems
  - Investigated atomizer parameters contributing to long-distance transportation of inhibitor particles.
  - Designed changing velocity fields in a straight pipe for more efficient production of training samples.
- 2.2: AI-assisted inhibitor optimization gathering and transportation pipelines
  - Built a neural network model mapping the velocity field into inhibitor deposition.
  - Established a probabilistic model to evaluate the reliability of the inhibitor protective film.

A comprehensive report detailing the tasks is provided in the appendix. Additionally, the presentation file for the quarterly report, prepared for the Technical Advisory Panel (TAP) members and PHMSA program managers, is also enclosed in the appendix.

### **Project Financial Activities Incurred during the Reporting Period:**

For Task 1, we supported 1 RA at ASU

For Task 2, we supported 1 RA at ASU

### **Project Activities with Cost Share Partners:**

Discussed with the Technical Advisory Panel members to solicit recommendations for our team's research activities.

### **Project Activities with External Partners:**

Conducted regular discussions with the Technical Advisory Panel, in addition to several separate meetings and email communications with individual advisory members.

### **Potential Project Risks:**

Nothing to report.

## **Future Project Work:**

For Task 1:

- Continue to investigate available and new techniques to develop inhibitor modification strategies
- Modifying selected candidates to enhance their inhibition efficacy

For Task 2:

- Build a Bayesian model for more efficient and adaptable risk assessment
- The extent of the developed AI-enhanced simulation model to consider different geometry information
- Investigate optical non-destructive testing and AI-based vision analysis methods to estimate inhibitor film thickness and coverage for improved reliability modeling
- Integrate additional experimental data into the inhibitor degradation model to better capture real-world complexities affecting inhibitor performance

We received comments/questions on the following technical areas.

1. Justification and literature reference to use brine water for testing.  
~ The team is working on justification and literature references for the motivation and support of brine water in the corrosion testing for gas pipelines. We will discuss detailed responses among the team and with our program manager. Updates will be provided in the next quarter's report.
2. Availability of inspection data and alternative data collection plans for risk assessment model.  
~ The team has reached out to all TAP members for help and suggestions. Meetings and discussions will be scheduled before the next quarter's report and detailed responses will be provided. The team is also planning to discuss with previous PHMSA project awardees for the related topic and obtain feedback/comments. Technical discussion meeting will be scheduled with the program manager before the next quarter report.

**Appendix 1**  
**Technical Progress Description for Task 1**

## Task 2. Quick screening of green inhibitors for gas pipeline protection

### 1.1 Introduction

Figure 1.1 illustrates the mechanism by which fatty acids inhibit corrosion through adsorption on metal surfaces. Fatty acids are amphiphilic molecules, meaning they have a polar (hydrophilic) head group and a nonpolar (hydrophobic) tail. The carboxylic acid group (-COOH) serves as the hydrophilic head, which has a strong affinity for metallic surfaces—particularly iron (Fe) in steel—where it forms chemical bonds (chemisorption) by interacting with surface  $\text{Fe}^{2+}$  or  $\text{Fe}^{3+}$  ions. This results in the anchoring of the molecule to the metal surface.

Once adsorbed, the long hydrocarbon tail (-CH<sub>2</sub>-...-CH<sub>3</sub>) of the fatty acid orients itself away from the surface and into the solution, forming a hydrophobic barrier layer. This monolayer prevents corrosive agents like water, oxygen, and chloride ions from reaching the metal surface, thereby inhibiting corrosion. This dual-function structure—anchoring head and shielding tail—is what makes fatty acids especially effective as environmentally friendly corrosion inhibitors in both aqueous and acidic environments.

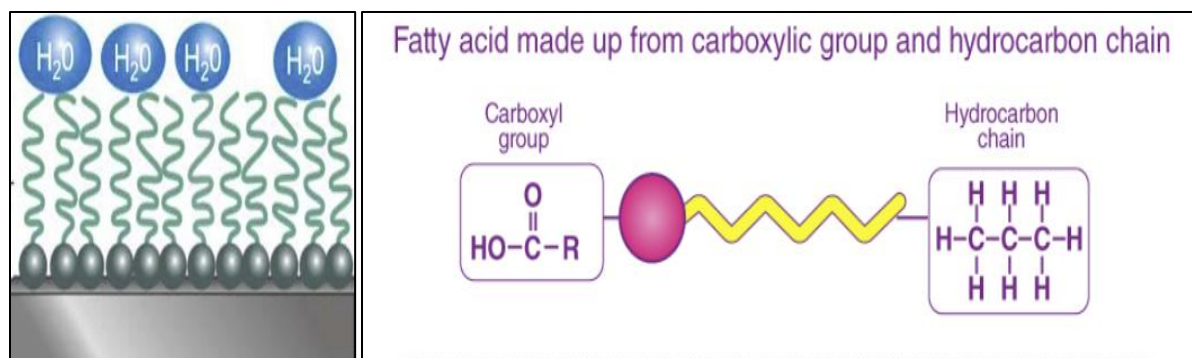


Figure 1.1. Mechanism of steel corrosion inhibition by free fatty acids.

The major fatty acids present in the hydrolyzed canola oil are listed in Table 1.1.

Table 1.1. Main fatty acids of hydrolyzed canola oil

Fatty Acid	Molecular Formula	Level of Saturation	Type of Bonds	Number of Double Bonds
Stearic acid	C <sub>18</sub> H <sub>36</sub> O <sub>2</sub>	Saturated	Only single bonds (C-C)	0
Palmitic acid	C <sub>16</sub> H <sub>32</sub> O <sub>2</sub>	Saturated	Only single bonds (C-C)	0
Oleic acid	C <sub>18</sub> H <sub>34</sub> O <sub>2</sub>	Monounsaturated	One double bond (C=C)	1
Linoleic acid	C <sub>18</sub> H <sub>32</sub> O <sub>2</sub>	Polyunsaturated	Two double bonds (C=C, C=C)	2

Stearic acid and palmitic acid are fully saturated, containing only single carbon–carbon (C–C) bonds, which makes them more stable and less reactive. Oleic acid, a monounsaturated fatty acid, contains one carbon–carbon double bond (C=C), introducing a kink in its structure that can affect its packing and adsorption behavior. Linoleic acid is polyunsaturated with two double bonds, making it more chemically reactive and potentially more effective in forming protective, flexible monolayers on metal surfaces. The variation in saturation levels and bond types among these fatty acids influences their physical properties and their ability to function as corrosion inhibitors.

Differences in soaps and fatty acids:

Free Fatty Acid (FFA) (-COOH group):

- Contains a carboxyl (-COOH) group, which is partially polar, but in water, it remains non-ionized mainly at neutral pH.
- The long hydrocarbon chain (hydrophobic tail) dominates, making FFAs predominantly hydrophobic and insoluble in water.

In soap, the carboxyl group is converted into a carboxylate salt (-COO<sup>-</sup>) by reacting with a strong base (NaOH or KOH).

- The carboxylate (-COO<sup>-</sup>) group is highly polar and ionized, which means it can interact strongly with water(dissolvable)

Soaps and surfactants both possess amphiphilic structures, meaning they contain a hydrophilic (water-attracting) head and a hydrophobic (water-repelling) tail, but their structural chemistry and behavior in water differ significantly. Soaps are typically derived from natural fatty acids, where the carboxyl group (-COOH) is converted into a carboxylate salt (-COO<sup>-</sup>) upon reaction with a strong base like NaOH or KOH. This gives soaps a negatively charged head, making them anionic in nature. However, soaps remain largely non-ionized at neutral pH and can become insoluble in hard water, leading to soap scum formation. On the other hand, synthetic surfactants like sodium dodecyl sulfate (SDS) and cetyltrimethylammonium bromide CTBA) have more stable and functional head groups—SDS is an anionic surfactant with a sulfate (-OSO<sub>3</sub><sup>-</sup>) head, while CTAB is a cationic surfactant featuring a quaternary ammonium (+NR<sub>4</sub>) head group. These surfactants are engineered to remain ionized in a wider range of conditions and are more effective in forming micelles and interacting with surfaces, making them widely used in industrial and corrosion-inhibition applications.

## 1.2 Methodology

### 1.2.1 Materials

Table 1.2 lists a diverse set of bio-based compounds that has been investigated for their corrosion inhibition performance, highlighting their chemical class and functional groups. Compounds such as pectin, a polysaccharide, contain functional groups such as carboxyl (-COOH) and hydroxyl (-OH), which can strongly adsorb onto metal surfaces and form protective films through hydrogen bonding or metal-ligand interactions. Surfactants such as CTAB and SDS fall under cationic and anionic classes, respectively, featuring quaternary ammonium, sulfate groups,

and long alkyl chains. These molecules function by creating a hydrophobic barrier on the metal surface, disrupting electrolyte contact and reducing corrosion reactions through electrostatic and physical adsorption.

Other compounds, such as hydrolyzed oil, palm oil, fatty acid methyl esters, and N-methyldiethanolamine (NMDEA), belong to triglyceride, ester, or amine classes, each carrying multiple functional groups like esters, hydroxyls, and fatty acid moieties. The oils and esters, especially those derived from oleic and stearic acids, contribute to corrosion inhibition via the formation of a compact, hydrophobic layer that blocks corrosive species. Fatty acids like oleic acid (monounsaturated) and stearic acid (saturated) offer both carboxyl and alkyl/alkene chains, which assist in strong surface binding and film formation. NMDEA provides lone pair electrons from the amine group and hydroxyls, enhancing adsorption onto metal substrates. Overall, these compounds inhibit corrosion through a combination of chemical adsorption, film formation, and electrostatic interaction, effectively reducing metal dissolution and surface attack.

Table 1.2. list of bio-based inhibitors that has been tested

Compounds	Class of Compounds	Functional Groups
Pectin	Polysaccharide	Carboxyl (-COOH) Hydroxyl (-OH) Ether (-C-O-C-)
CTAB (Cetyltrimethylammonium Bromide)	Cationic surfactant	(-N <sup>+</sup> (CH <sub>3</sub> ) <sub>3</sub> ), Quaternary Ammonium ,Alkyl chain
SDS (Sodium dodecyl sulfate)	Anionic surfactant	Sulfate (-OSO <sub>3</sub> <sup>-</sup> ), Alkyl chain
Hydrolyzed oil	Triglyceride (Mixture of fatty acids attached to glycerol molecule)	Stearic, oleic, palmitic, linoleic acids attached to a glycerol backbone
Fatty acid methyl esters	esters	Ester (-COOCH <sub>3</sub> ) Alkyl (-C-H, -CH <sub>2</sub> , -CH <sub>3</sub> )
NMDEA	Tertiary amine	(-N(CH <sub>3</sub> ), Hydroxyl (-OH))
Palm oil	Triglyceride	Fatty acids with Glycerol backbone
Stearic acid	Free fatty acid (saturated)	Carboxyl (-COOH) Alkane (-C-C-) single bond
Oleic acid	Fatty acid (monosaturated)	Carboxyl (-COOH)) Alkene (-C=C) one double bond

In this quarter, various compounds were utilized as green inhibitors for corrosion inhibition tests, sourced from different suppliers to ensure reproducibility and consistency in quality. Pectin, CTAB, SDS, NMDEA, stearic acid, and oleic acid were purchased from Sigma-Aldrich. The hydrolyzed oil used was produced in-house by hydrolyzing canola oil, allowing for controlled experimental conditions. Fatty acid methyl esters were derived from hydrolyzed oil by transesterification with methanol. Lastly, the palm oil was obtained from a food-grade commercial source.

### 1.2.2 Modification of Hydrolysed Oil

The transesterification reaction is a key chemical process used to convert triglycerides, commonly found in vegetable oils like canola oil, into fatty acid methyl esters (FAMES) and glycerol. This reaction involves reacting the triglyceride with a short-chain alcohol such as methanol or ethanol, in the presence of a basic catalyst like KOH or NaOH. The process yields

FAMEs, which are the main constituents of biodiesel, and glycerin as a byproduct. Beyond their use as biofuels, FAMEs are gaining attention as green corrosion inhibitors due to their surface-active properties.

Reactants: Triglycerides and methanol

Catalyst: KOH

Product: Transesterified fatty acid methyl esters

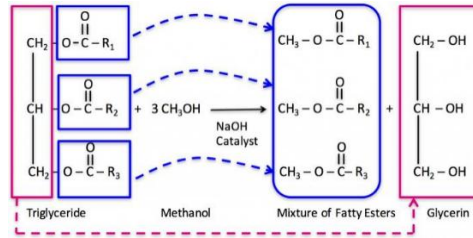


Figure 1.2 Chemical reaction for transforming canola oil into fatty acid methyl esters

The following describes the method employed to produce fatty acid methyl esters:

### Production

The transesterification process uses a 6:1 molar ratio of methanol to triglyceride. The amount of methanol required is calculated as follows:

#### 1.2.2.1 Calculation:

- Molecular weight of triglyceride (approximate for canola oil) = 929 g/mol
- Molecular weight of methanol = 46 g/mol
- Mass of oil = 50 g
- Molar ratio = 6:1 (methanol:triglyceride)

$$\frac{50 \text{ g oil}}{929 \text{ g/mol}} = \frac{x \text{ g methol}}{6 * 46 \text{ g/mol}}$$

Solving

for

x,

$$x = \frac{50 * 6 * 46}{929} \approx 15.85 \text{ g}$$

Thus, 14.85 g of methanol is required.

#### 1.2.2.2 Reaction Procedure:

- Weigh 1 g of potassium hydroxide (KOH) into an Erlenmeyer flask.
- Add 14.85 g of methanol to the flask.
- Stir the mixture until the KOH fully dissolves.

- Weigh 50 g of oil and add it to the KOH-methanol solution.
- Cover the flask with aluminum foil to prevent methanol evaporation.
- Stir the mixture for 60 minutes at 60°C.

### 1.2.2.3 Separation and Purification

After transesterification, the reaction mixture contains biodiesel (fatty acid methyl esters) and glycerol as a byproduct.

*Separation:*

- Glycerol, being denser, settles at the bottom of the reactor.
- The biodiesel-rich upper layer is carefully decanted.

*Purification Steps:*

- Flash evaporation: Heat the biodiesel layer briefly to vaporize residual methanol.
- Water washing: Dilute the biodiesel with water to extract any remaining methanol, followed by separation of the water layer.

### 1.2.2.4 Application

The resulting transesterified fatty acid methyl esters (biodiesel) can be utilized as a corrosion inhibitor.

## 1.2.3 Electrochemical Corrosion Testing

For corrosion testing and validation, the inhibitors were subjected to thorough testing in hydrochloric acid (HCl). The testing framework included electrochemical impedance spectroscopy (EIS), Tafel polarization, static weight loss measurements, EIS and Tafel polarization provided essential insights into the electrochemical behavior of the inhibitors, particularly their ability to reduce corrosion currents and enhance charge transfer resistance. Static weight loss tests measured the mass loss of carbon steel samples over time, offering a direct indication of the inhibitors' efficiency in mitigating corrosion under HCl media. The selected 10 inhibitors were tested.

### 1.2.3.1 Electrochemical Impedance Spectroscopy (EIS)

The interpretation of EIS data is typically facilitated using Nyquist and Bode plots, which graphically represent the impedance characteristics of the system. These plots can reveal:

- **Charge Transfer Resistance:** Related to the ease with which electrons can move across the electrode/electrolyte interface.
- **Double Layer Capacitance:** Reflects the capacitive behavior at the interface, influenced by the thickness and properties of the electrochemical double layer.
- **Warburg Impedance:** Indicates diffusion-controlled processes, often seen in porous coatings or corrosion layers.

Electrochemical Impedance Spectroscopy (EIS) tests were conducted to evaluate the efficiency of the shortlisted corrosion inhibitors. These tests were performed in ten different media:

- **Medium 1 (Control):** 1M HCL solution (control sample)
- **Medium 2:** 1M HCL with 2g per liter Pectin
- **Medium 3:** 1M HCL with 2g per liter CTAB
- **Medium 4:** 1M HCL with 2g per liter SDS
- **Medium 5:** 1M HCL with NMDEA dip
- **Medium 6:** 1M HCL with Hydrolyzed oil Dip
- **Medium 7:** 1M HCL with Fatty acid methyl esters Dip
- **Medium 8:** 1M HCL with Stearic acid Dip
- **Medium 9:** 1M HCL with Oleic acid Dip
- **Medium 10:** 1MHCL with Palm oil Dip

The EIS measurements utilized a standard three-electrode cell setup:

- **Working Electrode:** A36 steel specimen polished and brushed using sandpaper to remove oxidable layer.
- **Reference Electrode:** Saturated calomel electrode (SCE).
- **Counter Electrode:** Platinum wire.

The Electrochemical impedance spectroscopy was performed utilizing a frequency response analyzer in conjunction with a potentiostat. This setup ensured precise maintenance of the electrode potential while recording the impedance response. A summary of the specific parameters employed during the EIS tests is presented in Table 1.3.

Table 1.3. EIS Test Parameters

Parameter	Value	Description
AC Signal Amplitude	10 mV	The amplitude of the alternating current signal.
Frequency Range	100 kHz to 10 mHz	The range over which impedance was measured.
Potentiostat Mode	Potentiostatic (constant potential)	Maintains a constant electrode potential during measurements.
Equilibration Time	At least 3 hours	Allows the system to stabilize before measurements.

EIS measurements commenced following a stabilization period, allowing the electrochemical system to achieve a steady state. Impedance data were collected over the designated frequency range to encompass the full electrochemical response.

The impedance data were analyzed by fitting them to an equivalent circuit model to extract key parameters such as solution resistance ( $R_s$ ), charge transfer resistance ( $R_{ct}$ ), and constant phase element (CPE). These parameters were derived from Nyquist plots, which graph the imaginary part of impedance ( $Z''$ ) against the real part ( $Z'$ ).

The equivalent circuit used for analyzing the impedance plots consisted of:

- **R1**: Solution resistance ( $R_s$ ).
- **R2**: Charge transfer resistance ( $R_{ct}$ ).
- **CPE1**: Impedance of the constant phase element.

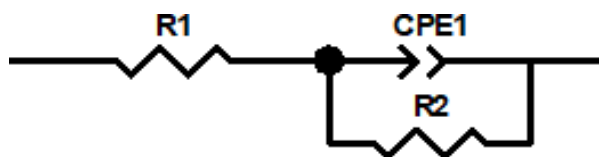


Figure 1.3. Equivalent Circuit Used for Analyzing the Impedance Spectra

### Steps for Measuring Solution and Charge Transfer Resistance

- 1) **Perform EIS Measurement**: Conduct an EIS experiment over a broad frequency range.
- 2) **Analyse Nyquist Plot**: Plot the Nyquist diagram and identify the intercepts and features corresponding to  $R_s$  and  $R_{ct}$ .
- 3) **Calculation of Parameters**:
  - **Solution Resistance ( $R_s$ )**: High-frequency intercept on the real axis of a Nyquist plot.
  - **Charge Transfer Resistance ( $R_{ct}$ )**: Represents the electron transfer resistance at the electrode-electrolyte interface.

#### 1.2.3.2 Tafel Polarization

##### Equipment Setup and Preparation

For the Tafel polarization test, a controlled electrochemical setup was utilized, typically comprising a potentiostat, a three-electrode cell, and software for data acquisition and analysis. The three-electrode system consisted of a working electrode (the metal under test), a reference electrode, and a counter electrode.

##### Stabilization of Open Circuit Potential (OCP)

The metal sample was immersed in the test solution, and the system was allowed to equilibrate to the open circuit potential (OCP). This step was crucial as it established a stable

baseline condition, for the electrochemical system. The OCP is the potential where the net current at the electrode surface is zero, indicating that the rates of the anodic and cathodic reactions have reached equilibrium.

### **Test Parameter Configuration**

The configuration of the test parameters was performed through the software interface of the potentiostat. Key parameters entered included:

- **Initial Potential ( $E_{\text{initial}}$ ):** Set 10 mV negative relative to the OCP. This was the starting point for the potential sweep.
- **Final Potential ( $E_{\text{final}}$ ):** Set 10 mV positive relative to the OCP. This defined the endpoint of the potential sweep.
- **Scan Rate:** Determined to be approximately 0.125 mV/s. The scan rate was crucial for ensuring that the system did not deviate significantly from equilibrium during the test.

### **Execution of the Potentiodynamic Polarization Tests**

Once the parameters were set, the potentiodynamic polarization test was initiated. The software controlled the potentiostat to apply a linear sweep of potential from the initial to the final set values. During this sweep:

- The potential was incrementally increased from  $E_{\text{initial}}$  to  $E_{\text{final}}$ .
- The current response of the system was continuously measured as the potential was varied.

### **Data Acquisition and Plotting**

The current and potential data collected during the tests were automatically recorded by the software. This data was used to generate the Tafel plot, which graphed the potential ( $E$ ) on the Y-axis versus the logarithm of the current density ( $\log I$ ) on the X-axis. The Tafel plot was essential for analyzing the electrochemical behavior of the metal under the test conditions

### **Identification of Linear Regions and Extrapolation**

The Tafel plot typically exhibited linear regions corresponding to the anodic and cathodic branches. These regions were critical for the analysis as they reflected the kinetics of the oxidation and reduction reactions. Using the software:

- The linear portions of the anodic and cathodic curves were identified.
- These linear regions were extrapolated back to their intersection at the corrosion potential ( $E_{\text{corr}}$ ).

### **Calculation of Corrosion Current Density ( $i_{\text{corr}}$ )**

The intersection points of the extrapolated anodic and cathodic lines provided the corrosion current density ( $i_{corr}$ ), which is a critical parameter directly related to the corrosion rate of the metal. Using specialized software,  $i_{corr}$  was converted into the corrosion rate by applying predefined constants and material properties, such as the metal's equivalent weight (EW) and density. Subsequently, the corrosion rate (CR) of the corrosion inhibitor was calculated using the following equation:

$$CR = \frac{i_{corr} K EW}{\rho A} \quad (1.1)$$

- **Medium 1 (Control):** 1M HCL solution (control sample)
- **Medium 2:** 1M HCL with 2g per liter Pectin
- **Medium 3:** 1M HCL with 2g per liter CTAB
- **Medium 4:** 1M HCL with 2g per liter SDS
- **Medium 5:** 1M HCL with NMDEA dip
- **Medium 6:** 1M HCL with Hydrolyzed oil Dip
- **Medium 7:** 1M HCL with Fatty acid methyl esters Dip
- **Medium 8:** 1M HCL with Stearic acid Dip
- **Medium 9:** 1M HCL with Oleic acid Dip
- **Medium 10:** 1MHCL with Palm oil Dip

#### 1.2.4 Static Weight Loss 1M HCL

The experiments, conducted over one week, assessed corrosion behavior under controlled conditions. To minimize oxygen exposure and ensure consistency, beakers were placed in a fume hood. Prior to immersion, each steel coupon was accurately weighed to establish its initial mass. Following the exposure period, the coupons were retrieved and meticulously cleaned to remove corrosion products. This involved scrubbing under running water with a bristle brush, followed by an acetone rinse. The coupons were then dried with acetone to remove residual moisture and reweighed to determine their final mass. Weight loss, calculated as the difference between initial and final masses, served as the primary metric for evaluating corrosion and comparing the protective effects of inhibitors, particularly pectin, in the test solutions. The study employed a harsh environment—1 M HCl as the corrosion medium—to identify the most effective inhibitors under extreme conditions.

### 1.3 Result and Discussion

#### 1.3.1 Electrochemical Corrosion Testing

##### 1.3.1.1 Electrochemical Impedance Spectroscopy (EIS) Results

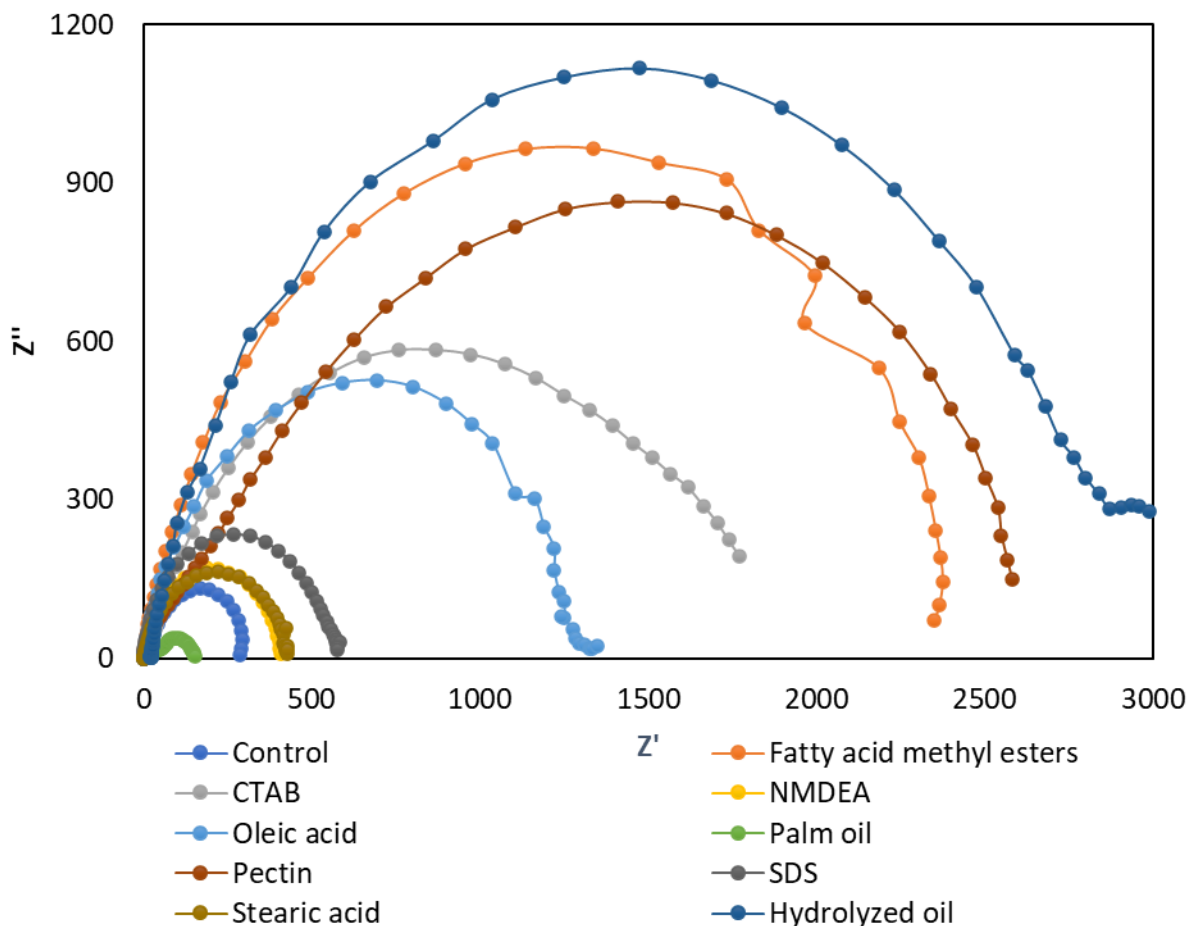


Figure 1.4. EIS Plot

Electrochemical impedance spectroscopy (EIS) results, presented in Figure 1.4, demonstrate varying inhibition efficiencies among the tested inhibitors. Hydrolyzed oil achieved the highest efficiency at 89.66%, with a polarization resistance ( $R_p$ ) of  $2889.3 \Omega \cdot \text{cm}^2$ , signifying excellent corrosion protection. Pectin followed closely, with an inhibition efficiency of 89.4% and an  $R_p$  of  $2818 \Omega \cdot \text{cm}^2$ , establishing it as a highly effective green inhibitor. Fatty acid methyl esters (FAMES) and CTAB also performed well, recording efficiencies of 85.5% and 83.67%, respectively, which suggest effective surface coverage and stable protective film formation.

In contrast, oleic acid exhibited a moderate inhibition efficiency of 74.9%, while NMDEA, SDS, and stearic acid showed lower efficiencies of 27.7%, 29.1%, and 29.6%, respectively, likely due to weaker adsorption or less stable protective layers. Notably, palm oil displayed a negative inhibition efficiency of -51.3%, indicating it may have exacerbated corrosion rather than inhibited it. Collectively, the data highlights a trend where esterified and mixed fatty acid systems, such as hydrolyzed oil and FAMES, outperform single-component inhibitors, likely owing to enhanced molecular interactions and synergistic effects in corrosion inhibition.

Table 1.4. EIS test results and associated inhabitation efficiency

Sample	Rs (solution resistance) ( $\Omega \text{ cm}^2$ )	RP (Polarization resistance) ( $\Omega \text{ cm}^2$ )	CPE (constant phase element) (F/s)	n	Inhibition efficiency (%)
Control	1.232	298.6	$8.8 * 10^{-4}$	0.83778	_____
Fatty acid methyl esters	0.95616	2095	$1.9 * 10^{-5}$	0.89975	85.5
CTAB	0.82195	1829	$1.6 * 10^{-4}$	0.69816	83.67
NMDEA	2.419	401.9	$2.7 * 10^{-4}$	0.89772	27.7
Oleic acid	0.98975	1189	$2.9 * 10^{-5}$	0.89824	74.9
Palm oil	5.993	145.47	$1.2 * 10^{-4}$	0.7458	-51.3
Pectin	0.88799	2818	$9.7 * 10^{-5}$	0.64739	89.4
SDS	0.79217	421	$1.3 * 10^{-4}$	0.89003	29.1
Stearic acid	1.967	418.3	$9.4 * 10^{-5}$	0.85581	29.6
Hydrolyzed oil	21.5	2889.3	$1.43 * 10^{-5}$	0.86	89.66

Electrochemical impedance spectroscopy (EIS) results highlight distinct inhibition efficiencies among the tested inhibitors. Hydrolyzed oil demonstrated the highest efficiency at 89.66%, with a polarization resistance ( $R_P$ ) of 2889.3  $\Omega \cdot \text{cm}^2$ , reflecting robust corrosion protection. Pectin closely followed, achieving an inhibition efficiency of 89.4% and an  $R_P$  of 2818  $\Omega \cdot \text{cm}^2$ , confirming its efficacy as a top-performing green inhibitor. Fatty acid methyl esters (FAMES) and CTAB also exhibited strong performance, with efficiencies of 85.5% and 83.67%, respectively, indicative of effective surface coverage and stable protective film formation.

Oleic acid displayed a moderate inhibition efficiency of 74.9%, whereas NMDEA, SDS, and stearic acid showed lower efficiencies of 27.7%, 29.1%, and 29.6%, respectively, likely due to weaker adsorption or less stable protective layers. Strikingly, palm oil recorded a negative inhibition efficiency of -51.3%, suggesting it accelerated corrosion rather than inhibited it. Overall, the data reveals that esterified and mixed fatty acid systems, such as hydrolyzed oil and FAMES, outperform single-component inhibitors, likely owing to enhanced molecular interactions and synergistic effects in corrosion inhibition.

### 1.3.1.2 Tafel Polarization

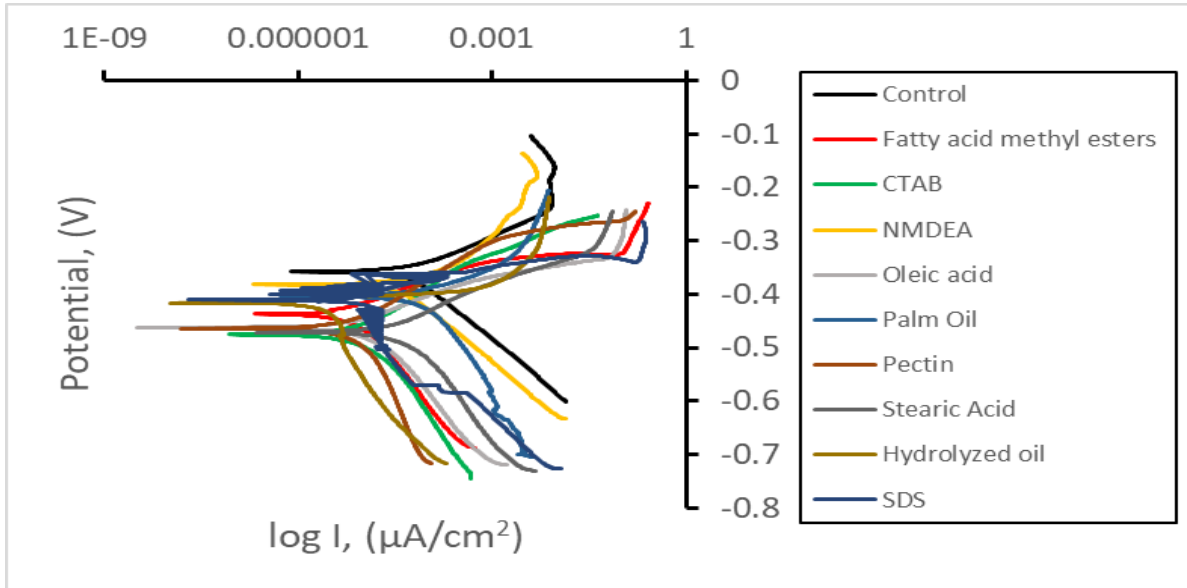


Figure 1.5. Tafel Polarization Plot

**Table 1.5** Tafel test results and associated inhabitation efficiency

Sample	$E_{corr}$ (mV)	$I_{corr}$ ( $\mu\text{A}/\text{cm}^2$ )	CR (mmpy)	Inhibition efficiency (%)
Control	-357	57.1	0.6603	-----
Fatty acid methyl esters	-436.7	7.551	0.0873	86.78
CTAB	-475.7	12.84	0.1485	77.51
NMDEA	-382.3	41.1	0.4753	28.02
Oleic acid	-462.5	11.81	0.1366	79.3
Palm oil	-404.05	119.33	1.38	-52.46
Pectin	-464.8	8.865	0.1025	84.45
Stearic acid	-471.2	40.18	0.4643	29.63
Hydrolyzed oil	-417.3	9.2	0.1064	83.89
SDS	-421.3	38.98	0.4508	31.73

Among the tested samples, fatty acid methyl esters and hydrolyzed oil exhibited the highest corrosion inhibition efficiencies at 86.78% and 83.89%, respectively. These were characterized by significantly reduced corrosion current densities ( $I_{corr}$ ) of  $7.551 \mu\text{A}/\text{cm}^2$  and  $9.2 \mu\text{A}/\text{cm}^2$ , and correspondingly low corrosion rates (CR) of 0.0873 mm/yr and 0.1064 mm/yr. Pectin also demonstrated strong performance as a green inhibitor, achieving an inhibition efficiency of 84.45%.

Oleic acid and CTAB showed moderate inhibition efficiencies of 79.3% and 77.51%, respectively, reflecting effective surface interactions and barrier formation. In contrast, NMDEA, SDS, and stearic acid exhibited lower efficiencies of 28.02%, 31.73%, and 29.63%, with elevated  $I_{corr}$  values exceeding  $38 \mu\text{A}/\text{cm}^2$ , indicative of weaker adsorption or less stable protective films. Most notably, palm oil displayed a negative inhibition efficiency of -52.46%, accompanied by a high  $I_{corr}$  of  $119.33 \mu\text{A}/\text{cm}^2$ , suggesting it exacerbated corrosion rather than mitigated it.

### 1.3.2 Static Weight Loss 1M HCl

Table 1.6 Static weight loss test results in 1M HCL and associated inhabitation efficiency

Inhibitor	Measured weight	Average	Weight Loss (g)	Corrosion (%)	Inhibitor Efficiency (%)
Control	Weight before corrosion	3.8205	0.5225	14	-
	Weight after corrosion	3.2980			
Hydrolysed oil	Weight before corrosion	3.7961	0.0578	2	88.91
	Weight after corrosion	3.7385			
Palm oil	Weight before corrosion	3.8083	0.5948	16	-14.22
	Weight after corrosion	3.2134			
Oleic Acid	Weight before corrosion	3.81203	0.2715	7	47.92
	Weight after corrosion	3.5405			
Stearic acid	Weight before corrosion	3.8064	0.3967	10	23.78
	Weight after corrosion	3.4096			
Fatty acid methyl esters	Weight before corrosion	3.8058	0.1381	4	73.47
	Weight after corrosion	3.6677			
NMDEA	Weight before corrosion	3.8165	0.0731	2	86.01
	Weight after corrosion	3.7434			
Pectin	Weight before corrosion	3.8125	0.0519	1	90.06
	Weight after corrosion	3.7606			
CTAB	Weight before corrosion	3.8178	0.05629	1	89.48
	Weight after corrosion	3.76152			
SDS	Weight before corrosion	3.79105	0.4968	13	4.28
	Weight after corrosion	3.2942			

The static weight loss test results confirm the effectiveness of various corrosion inhibitors, as determined by the weight loss of metal specimens after exposure. Pectin exhibited the highest inhibition efficiency at 90.06%, followed closely by CTAB (89.48%), hydrolyzed oil (88.91%), and NMDEA (86.01%). These inhibitors limited weight loss and corrosion to 1–2%, demonstrating robust protective capabilities. Fatty acid methyl esters also performed well, achieving a 73.47% inhibition efficiency, while oleic acid showed moderate efficacy at 47.92%, likely due to incomplete surface adsorption. In contrast, stearic acid (23.78%) and SDS (4.28%) displayed poor performance, with significantly higher weight loss and corrosion rates. Palm oil exhibited a negative inhibition efficiency (-14.22%), suggesting it may have accelerated corrosion rather than mitigated it. The control sample, lacking any inhibitor, experienced a high corrosion rate (14%) and weight loss (0.5225 g), underscoring the severity of unprotected corrosion. These weight loss findings correlate strongly with electrochemical data, supporting the conclusion that multifunctional, surface-active inhibitors—such as pectin, CTAB, and hydrolyzed oil—are highly effective at reducing corrosion.

### 1.3.3 Promising Green Inhibitor Candidates

Based on screening test results from the past six quarters, we recommend the following promising green inhibitors for further development and evaluation in this project:

- Fatty acids and their derivatives: These compounds have shown potential as sustainable corrosion inhibitors.
- Pectin and its derivatives: Naturally occurring polysaccharides with promising inhibitory properties.
- Surfactants: Surface-active agents exhibiting favorable performance in initial tests.

## **1.4 Multi-Compound Green Corrosion Inhibitor for Gas Pipeline: Synthesis, Optimization, and Evaluation (GTI's Efforts)**

### **1.4.1 Executive summary**

Green corrosion inhibitors are eco-friendly substances designed to prevent or reduce the corrosion of oil and gas-transporting pipelines. They offer a sustainable and safer alternative to conventional chemical inhibitors due to their biodegradability and non-toxicity, thus they are less harmful to ecosystems.

In the previous reporting period, we exploited 26 natural products and enzymes to identify candidate inhibitors with the potential to coat the surface of steel and inhibit general corrosion. We selected the 5 products that resulted in the lowest weight losses and further tested their ability to inhibit corrosion using carbon steel beads in 24-well plates. The corrosion inhibitors were serially diluted using a 1 M HCl solution to form a concentration gradient and determine the lowest concentration of inhibitor required to reduce corrosion levels. The effects of the concentration gradient were visible in the weight losses of each inhibitor, validating the usage of *Pseudomonas putida* organic extract, Moringa Oleifera leaf extract, food waste extract, putrescine, and protease from bovine pancreas as good candidates for corrosion inhibition.

Future studies will be focused on corrosion inhibition testing of the best candidate substances using carbon steel coupons and electrochemical testing under conditions that mimic gas-transporting pipelines.

### **1.4.2 Background**

Green corrosion inhibitors are eco-friendly substances designed to prevent or reduce the corrosion of oil and gas-transporting pipelines, offering a sustainable and safer alternative to conventional chemical inhibitors. The substances are mainly derived from natural sources such as plants, animals, microorganisms, essential oils, and biopolymers. Similar to conventional chemical corrosion inhibitors, they work by forming a protective film on the surface of metals and act as a barrier against corrosive agents such as oxygen, carbon dioxide, hydrogen sulfide, moisture, and aggressive chemicals. Green corrosion inhibitors contribute to environmental sustainability solutions due to their biodegradability and non-toxicity, making them less harmful to ecosystems compared to the chemical-based inhibitors (Khan et al., 2022). These properties make them a promising alternative to conventional corrosion inhibitors. Green inhibitors are also selected to meet stringent environmental regulations and sustainability goals. The use of green corrosion inhibitors is becoming increasingly popular in industries such as oil and gas, water treatment, and construction sectors.

### **1.4.3 Project objective**

The general objective of this project is to identify and test green corrosion inhibitors for controlling the corrosion of gas-transport pipelines.

The specific objectives of the project include:

1. Identification of enzymes or natural products for corrosion inhibition.
2. Laboratory-based synthesis of green corrosion inhibitors.
3. Testing of the products' corrosion inhibitory activities.

#### **1.4.4 Corrosion inhibitor testing**

. To evaluate the corrosion inhibitory activities of candidate inhibitors, carbon steel (C1018) ball bearings (Grainger, hardness C60 to C67, Grade 200) were used in microtiter plates. Because of their small size ( $55.0 \pm 0.3$  mg,  $\phi = 0.238 \pm 0.001$  cm,  $A = 0.178$  cm<sup>2</sup>) and increased surface area of exposure, these ball bearings were ideal for large scale screening in small volume in microtiter plates [1]. Beads were pretreated according to the National Association of Corrosion Engineers (NACE) protocol RP0775-2005, which involved sanding the beads using sandpaper by rolling them between two sheets of grit size 220 or 300 sandpaper for several minutes. The beads were then rinsed in isopropyl alcohol and left to dry overnight under air stream. Beads were sorted into pairs and weighed. Corrosion inhibitory activities were performed in 24-well plates containing 2 mL of 1 M HCl solution in deionized water and different concentrations of candidate corrosion inhibitors.

The corrosion inhibitors that minimized the corrosive impacts of the HCl solution from the initial screening process included food waste organic extract, *Pseudomonas putida* (*P. putida*) organic extract, Moringa organic extract, putrescine, and protease. The extraction processes of the active compounds for the laboratory-based products were the same as previously reported. Serial dilutions of these inhibitors were made using 1 M HCl solution. The following concentration gradient (in mM) was used for putrescine, whose molecular weight is known: 50, 25, 10, 5, 1, 0.5, 0.25, and 0.1. For protease and the laboratory-produced products, the following concentration gradient [in part per million (ppm)] was used: 1,000, 750, 500, 250, 100, 50, 25, and 10.

Bead pairs without the inhibitors were used as controls. Triplicate wells containing two beads per well were used for each sample. The microtiter plate wells were sealed with microtiter sealing films, covered with lids, and incubated under anaerobic conditions in a Coy anaerobic hood filled with 10% CO<sub>2</sub> in nitrogen. The plates were incubated at 30°C for 14 days. At the end of the incubation period, the bead pairs were removed from the microtiter plates and cleaned by sonicating in a 15% HCl solution containing 5 g/L of corrosion inhibitor 1,3-di-n-butyl-2 thiourea (DBT) for 2 minutes, sonicating in 1 M NaHCO<sub>3</sub> for 2 minutes, submerging in deionized water, and sonicating in isopropyl alcohol for 2 minutes. The bead pairs were allowed to dry under air stream and weighed to obtain final weights.

#### **1.4.5 Corrosion inhibitor screening**

The average weight changes in the bead pairs incubated with the highest concentrations of inhibitors after 14 days of incubation ranged from a weight loss of 38-46 mg. The lowest weight losses were observed in putrescine and the *P. putida* organic extract. In comparison, an average weight loss of around 55 mg were observed in the controls (1 M HCl with no inhibitors added).

The effects of the gradient concentrations on the inhibitors were apparent in the bead pair weight losses, as higher concentrations of inhibitors resulted in lower weight losses. Increased weight losses were observed as the concentration of inhibitors decreased. The most consistent gradients were observed in the lab-produced organic extracts. Apparent inhibition was observed at a concentration of at least 500 ppm for all the inhibitors.

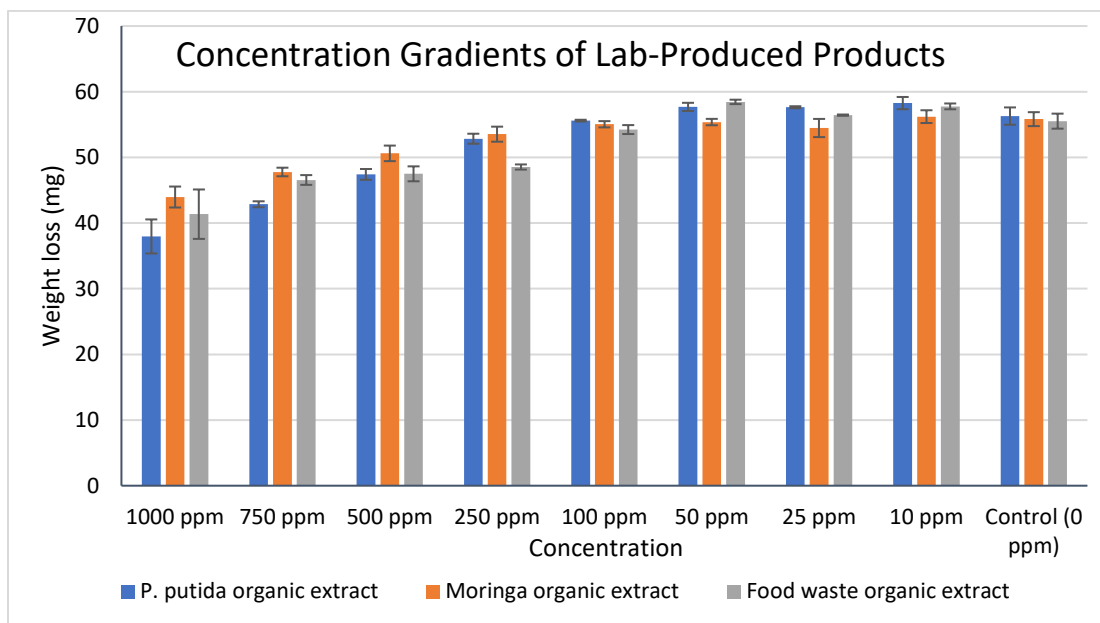


Figure 1.6 Changes in the weight of bead pairs in 1 M HCl solution in the presence of lab-produced candidate corrosion inhibitors. Each bead pair was weighed after the cleaning process, and the average weight change was graphed.

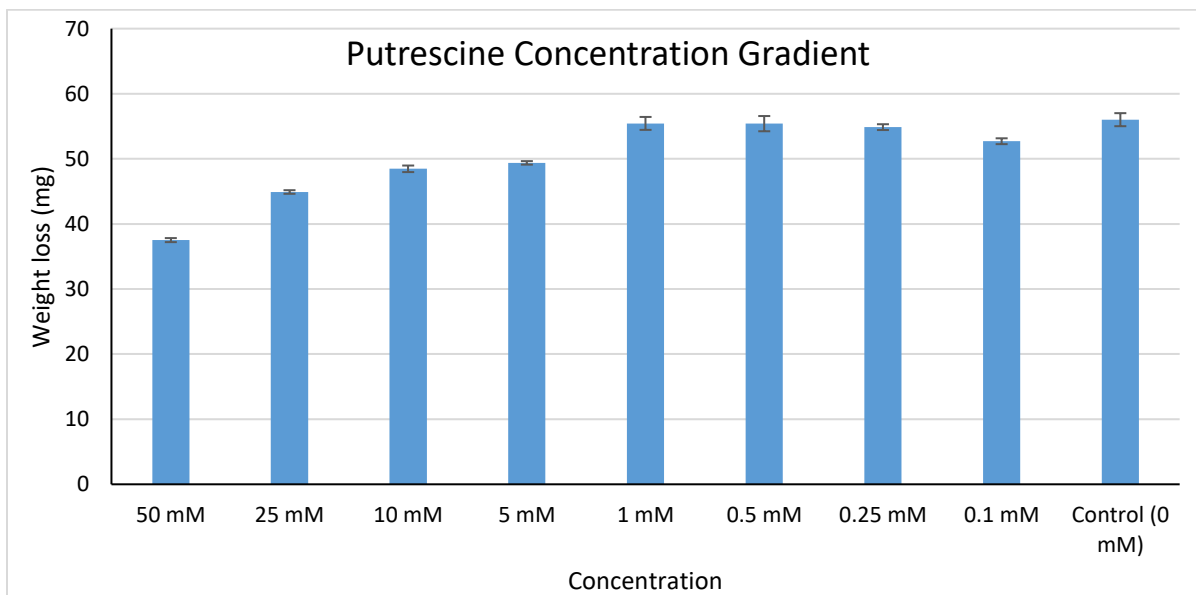


Figure 1.7 Changes in the weight of bead pairs in 1 M HCl solution in the presence of different concentrations of putrescine.

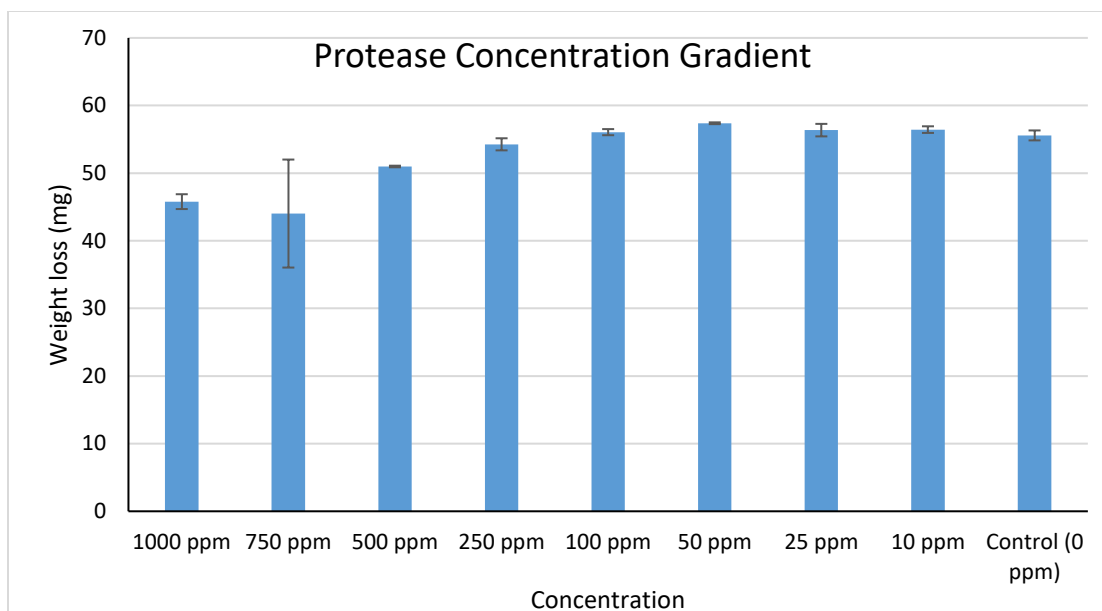


Figure 1.8 Changes in the weight of bead pairs in 1 M HCl solution in the presence of different concentrations of protease (from bovine pancreas).

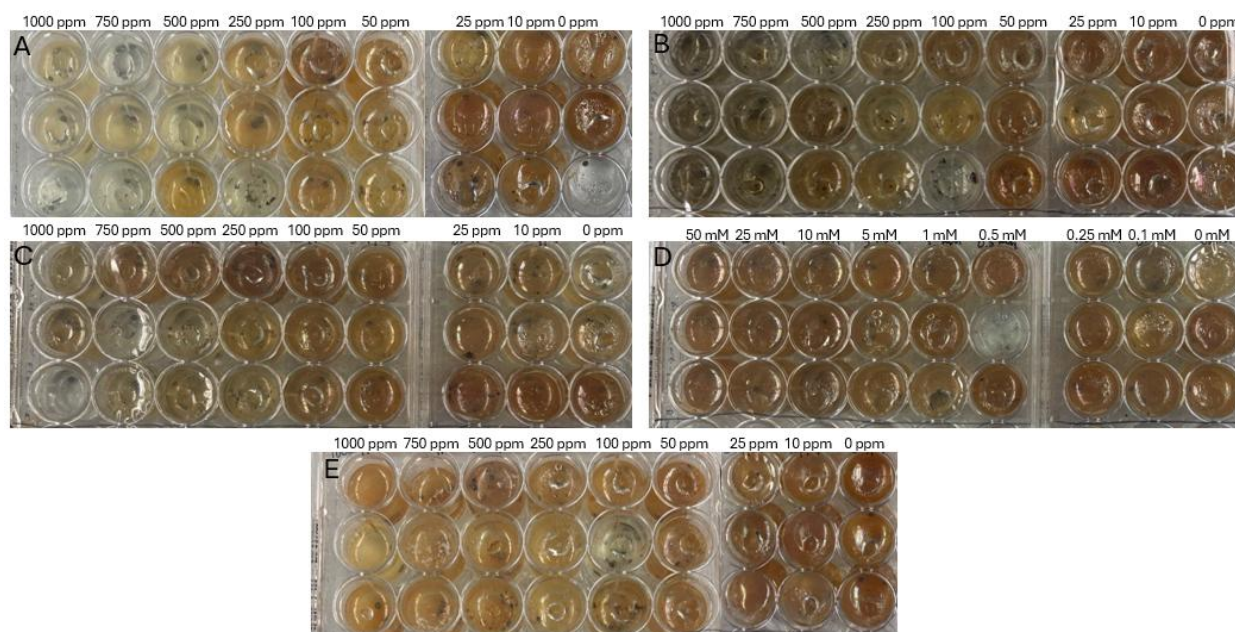


Figure 1.9 *P. putida* organic extract (A), Moringa organic extract (B), food waste organic extract (C), putrescine (D), and protease (E) concentration gradient plates after 14 days of incubation, with visible signs of corrosion.

The concentration gradient weight loss data confirms the efficacy of these candidate green corrosion inhibitors. The following formula was used to determine inhibition efficiency, where corrosion rate was chosen to be the weight loss.

$$\text{Inhibition Efficiency} = \frac{\text{Corrosion Rate}_{\text{inhibitor}} - \text{Corrosion Rate}_{\text{control}}}{\text{Corrosion Rate}_{\text{control}}} \times 100$$

Table 1.7 Summarized inhibition efficiencies for each corrosion inhibitor. Inhibition efficiencies were calculated based on their respective controls, and values are listed as percentages (%).

Concentration (ppm / mM)	Inhibition efficiency				
	<i>P. putida</i> organic extract	Moringa organic extract	Food waste organic extract	Protease	Putrescine *
1000 / 50	32.57 ± 4.60	21.25 ± 2.86	25.52 ± 6.78	17.62 ± 1.97	33.03 ± 0.55
750 / 25	23.86 ± 0.81	14.41 ± 1.17	16.14 ± 1.34	20.79 ± 14.36	19.84 ± 0.49
500 / 10	15.78 ± 1.46	9.33 ± 2.12	14.45 ± 2.05	8.27 ± 0.21	13.48 ± 0.90
250 / 5	6.12 ± 1.36	4.10 ± 2.05	12.58 ± 0.70	2.37 ± 1.61	11.85 ± 0.48
100 / 1	1.23 ± 0.23	1.40 ± 0.85	2.31 ± 1.22	-0.87 ± 0.81	1.02 ± 1.77
50 / 0.5	-2.49 ± 1.10	0.80 ± 0.88	-5.28 ± 0.61	-3.24 ± 0.23	1.09 ± 2.09
25 / 0.25	-2.39 ± 0.27	2.42 ± 2.48	-1.65 ± 0.17	-1.40 ± 1.66	2.05 ± 0.80
10 / 0.1	-3.51 ± 1.66	-0.68 ± 1.74	-4.05 ± 0.80	-1.54 ± 9.69	5.91 ± 0.80

\*Concentrations used are in mM

The inhibition efficiency of protease was reduced (resulted in a negative value) at a concentration of 100 ppm and lower. The inhibition efficiency was reduced at 50 ppm and lower for *P. putida* organic extract and food waste organic extract, and 10 ppm and lower for Moringa organic extract. Putrescine was able to show inhibition efficiency at all concentrations compared to its control even at a 0.1 mM concentration.

Controls showed a bead pair weight loss of 51% over the 14-day incubation period. In comparison, the highest concentrations of corrosion inhibitors resulted in a weight loss of 35-43%. Overall, the minimum inhibitory concentration that shows consistent positive inhibition appears to be 100 ppm for the lab-produced inhibitors, 250 ppm for protease, and 5 mM for putrescine.

Future research will involve selecting the minimum inhibitory concentrations that show inhibitory activities of the selected inhibitors and use these for testing on weight loss using carbon steel coupons, as well as electrochemical testing in brine solution that mimics natural gas fluid constituents.

## References

1. Fida T T, Sharma M, Shen Y, et al. Microbial sulfite oxidation coupled to nitrate reduction in makeup water for oil production[J]. Chemosphere, 2021, 284: 131298.
2. Khan M A A, Irfan O M, Djavanroodi F, et al. Development of sustainable inhibitors for corrosion control[J]. Sustainability, 2022, 14(15): 9502.

**Appendix 2**  
**Technical Progress Description for Task 2**

## **Task 2. Simulation-based Inhibitor Implementation Optimization in Gas Gathering and Transportation Pipelines**

### **2.1 Introduction**

#### **2.1.1 Background**

In the long-term operation of natural gas pipelines, applying corrosion inhibitors as a protective film on the pipe wall is one of the methods to prevent internal corrosion in the pipeline. However, they are not widely adopted in the pipeline industry, especially for gas pipelines, due to concerns of cost, toxicity, and compatibility with the gas. By forming a protective film on the pipe wall, corrosion inhibitors reduce the impact of corrosive agents such as CO<sub>2</sub> and H<sub>2</sub>S on the metal surface, thereby extending the service life of the pipeline. However, the protective capability of the pipe wall is not constant and is influenced by multiple factors, among which the degradation of corrosion inhibitors is a primary cause of protection loss. Extensive literature suggests that even pipelines treated with inhibitors exhibit increasing corrosion over time, providing indirect evidence of the inhibitors' gradual degradation. Over time, corrosion inhibitors gradually degrade, eventually requiring replenishment to maintain effective protection. Existing studies mainly focus on the overall application effectiveness of corrosion inhibitors, yet there is still a lack of systematic research on their degradation mechanisms, localized protective variations, and strategies for optimizing replenishment. Therefore, establishing a predictive model for pipeline wall protection reliability, which comprehensively accounts for inhibitor degradation characteristics, localized corrosion environments, and fluid dynamics, is of significant engineering importance for ensuring the long-term operational safety of pipelines.

In the previous study, a numerical simulation framework was developed to predict the distribution of corrosion inhibitors under given injection conditions. The primary focus was on establishing a mapping between the injected inhibitor particles and their deposition on the pipe wall. This framework provided an efficient way to assess inhibitor distribution and optimize injection parameters. However, due to the complexity of pipeline systems, the movement of inhibitor particles is influenced by the nearby flow field in the pipeline, fluid dynamics, and environmental factors, making precise modeling challenging. Even though CFD simulations can provide high-fidelity predictions, they require substantial computational resources, particularly when considering long-distance transportation and varying pipeline configurations. Thus, improving the prediction accuracy while reducing computational costs remains a key challenge.

Moreover, while the previous study used inhibitor deposition as an indicator of inhibitor effectiveness, deposition alone does not fully determine the protective capability of the inhibitor. Since the inhibitor degrades over time, its ability to prevent corrosion diminishes, thereby increasing the risk of pipeline deterioration. Consequently, predicting initial deposition through CFD is insufficient for a comprehensive evaluation of pipeline protection reliability. In real-world applications, localized corrosion intensification is often observed as inhibitors degrade, leading to a reduction in overall protective effectiveness. Therefore, the replenishment strategy of inhibitors

should not only be based on a global assessment but should also consider localized corrosion severity, inhibitor degradation rates, and fluid flow characteristics, which have not been adequately addressed in the current simulation framework.

To address these challenges, this study extends the existing CFD-based modeling approach to construct a more efficient and adaptable inhibitor deposition model under varying flow conditions. Furthermore, a probabilistic degradation model will be developed to explore pipeline protection failure mechanisms, allowing for improving protective efficiency in high-risk regions. Through refined prediction and strategic replenishment, the study aims to ensure that the pipeline remains within safe corrosion limits over extended operational periods.

### **2.1.2 Objectives**

As depicted in Figure 2.1, the primary objective of this study is to develop a probabilistic failure assessment framework for corrosion inhibitors and optimize injection strategies to enhance long-term pipeline protection. The research consists of four main stages:

1) First, CFD (Computational Fluid Dynamics) simulations are employed to generate high-quality sample data, simulating the transport and deposition of inhibitor particles under various flow conditions. By selecting representative sampling regions within the simulation domain, particle trajectories and wall deposition points are extracted to form the input-output dataset for model training.

2) Second, based on the generated dataset, a probabilistic deposition prediction model is constructed. This model leverages a neural network architecture incorporating Fourier layers and encoders to take flow velocity fields as input and predict the probabilistic distribution of particle-wall deposition. This enables efficient and accurate prediction of inhibitor behavior in complex pipeline networks.

3) Building on the deposition model, the study further develops a probabilistic inhibitor degradation model that captures time-dependent efficiency decay. Using the initial deposition-derived efficiency as input, a probabilistic framework incorporating Bayesian updating is employed to simulate the degradation process and quantify variations in inhibitor performance across different samples and operating conditions.

4) Finally, by integrating possible future inspection data, the model can be updated to dynamically assess the risk of pipeline failure. It should be noted that most of the gas pipelines do not have corrosion inhibitors implemented to mitigate internal corrosion. The existing inspection data obtained from pipeline inspection is likely to have no corrosion inhibitor. Thus, the current focus is on the methodology demonstration to show that, in a simulated scenario, the inspection data can effectively reduce the uncertainty and enhance the prediction confidence. Through Monte Carlo simulation and uncertainty propagation, the study estimates the probability of the system reaching a critical corrosion state at future time points, thereby providing quantitative decision

support for optimizing inhibitor injection strategies.

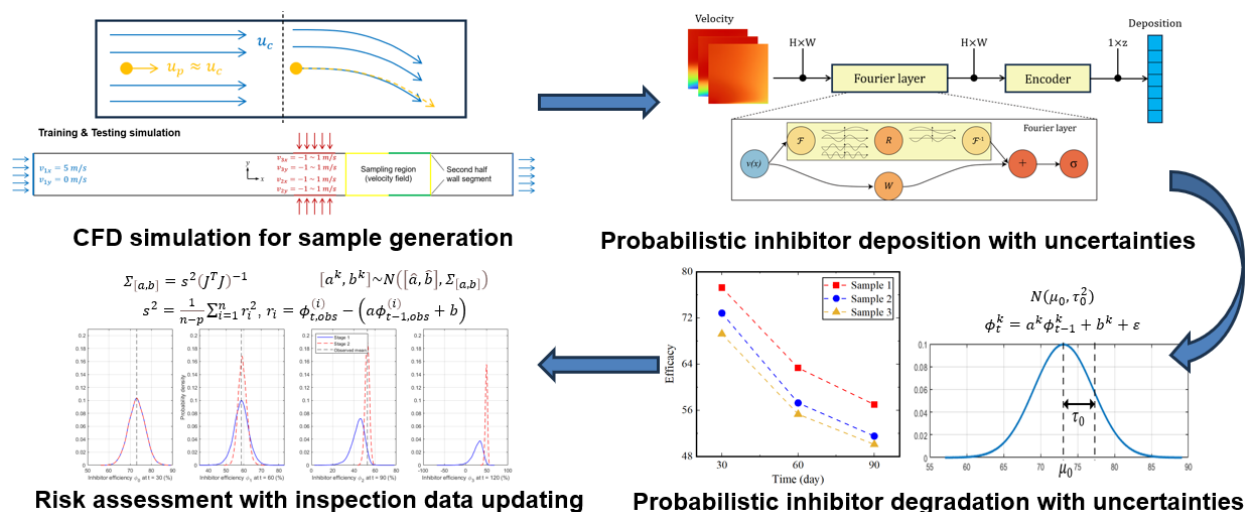


Figure 2.1: Illustration of the workflow of Task 2 in Q6.

## 2.2 Methodology

### 2.2.1 AI-enhanced CFD for inhibitor deposition prediction

In this study, we focus on predicting inhibitor deposition under the long-distance transport of corrosion inhibitor particles within the pipeline. By carefully tuning the parameters of the atomizer, sufficiently small particles with low inertia can be generated. This configuration ensures a wide distribution of the inhibitor over extended distances, improving its effectiveness in corrosion protection. Under these conditions, the particles are predominantly carried by the continuous phase that avoids settling prematurely. Figure 2.2 gives an example that particle velocity  $u_p$  quickly adjusts to particle velocity  $u_c$  when facing flow field change. At this point, the particle deposition can be considered dependent on the nearby flow field.

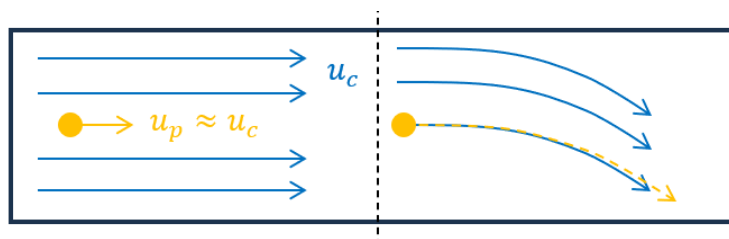


Figure 2.2: Illustration of the workflow of Task 2 in Q6.

Building upon the above foundation, the objective of this section is to efficiently predict inhibitor particle deposition during pipeline transport by integrating machine learning with CFD simulations, which serves as a basis for the reliability modeling in the subsequent section. Under this framework, conventional CFD simulation requires numerous parameters and structural factors, such as the fluid properties of the continuous phase and the geometric configuration of the pipeline, resulting in significant computational costs. To address this challenge, we incorporate machine learning techniques to enable more efficient deposition predictions across diverse operating

conditions. The following subsections will respectively introduce the simulation setup and the AI-enhanced method in detail.

### 2.2.1.1 Simulation setup

In CFD simulations, we mainly focus on deposition prediction with given velocity fields. This serves as the basis for further research on geometry change in the pipeline. For example, pipeline bends are prone to top-of-the-line corrosion (TLC) [1], which is generally caused by condensation of corrosive vapor on the top pipe wall. Currently, CFD simulations are performed in a straight pipe with various velocity fields.

To simplify the implementation, we assume that only the flow region near the corrosion-prone area can affect the particle deposition. This is based on the attenuation of flow characteristics during the transportation process. Under such an assumption, we generate training and testing data in a straight pipe, as shown in Figure. 2.3. A sampling region is marked in the figure, in which the velocity field is used as the input of the prediction model. Two additional velocity inlets are set in the pipe to randomly adjust the velocity field of the sampling region. Besides, the deposition of the second half wall segment in this region is also collected as the prediction target. With this configuration, different types of velocity fields are collected from the one pipe system to save the computational cost from repeated modelling and meshing implementations.

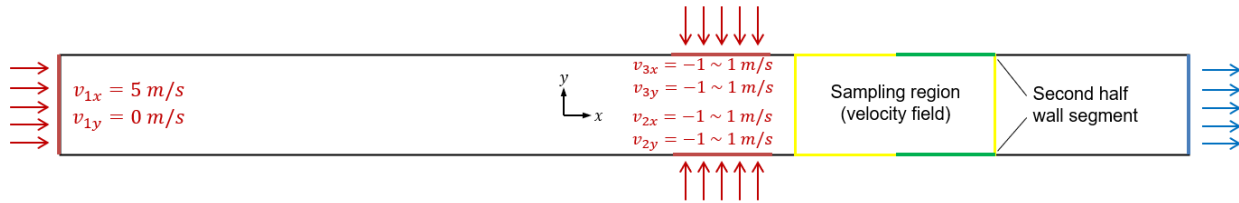


Figure 2.3: Illustration of data sampling in the straight pipe.

It is noted that particle deposition is also related to the time, which can be roughly recorded when the first batch of injected particles arrive at the corrosion-prone area. Due to the simple proportional relationship among different deposition times shown in Figure 2.4, we only focus on predicting deposition in a fixed time interval in this study. Considering the distance from the injection point to the sampling region is different in training and testing cases, corresponding time step numbers are adjusted in each case to ensure similar deposition time.

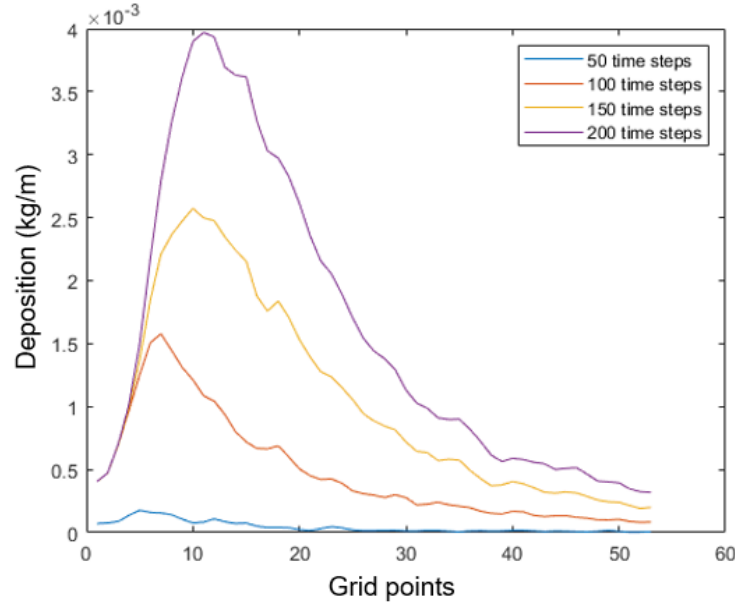


Figure 2.4: Comparison of particle deposition under different calculation time steps in a case.

With the utilization of DPM, some detailed settings for training and testing cases are identical, as described below

- **Meshing and grid point data:**
  - **General size:** In the currently considered low-speed steady flow, the edge sizing is configured with a uniform cell length of 10 mm, in which the flow solution can still converge.
  - **Sampling region data:** Both training and testing cases adopt the sampling region with the same number ( $51 \times 101$ ) of grid points.
- **Phase Properties:**
  - **Continuous phase:** Methane gas is considered as the only continuous phase with the density of  $0.656 \text{ kg/m}^3$  and the viscosity of  $0.01 \text{ MPa}\cdot\text{s}$  ( $25^\circ\text{C}$ ).
  - **Discrete phase:** Inhibitor injection is simulated by the flat-fan atomizer in DPM. Inhibitors are regarded as inertia oil-like particles with the density of  $770 \text{ kg/m}^3$  and the viscosity of  $50 \text{ MPa}\cdot\text{s}$  ( $25^\circ\text{C}$ ).
- **Solution settings:**
  - **Viscous model:** The viscous model is related to the exchange of momentum, energy, and concentration among fluid media, which influence flow dynamics and computational WSS results. The  $k-\omega$  model is used to simulate flow viscous.
  - **Discrete phase model:** DPM provides calculation of particle injection and interaction with the continuous phase. The involved erosion model is opened to record particle properties on the pipe wall.

- **Particle injection:** In DPM, the flat-fan atomizer is used to simulate particle injection in this case. Appropriate adjustment in the orifice width of the atomizer can contribute to particles' long-distance transportation. With the properties of particles and continuous phase in this study, the orifice width is set to 2E-8 m.
- **Solution method:** The “Coupled” method is applied that solves momentum and continuity equations in a tightly coupled manner. This can accelerate the convergence of the solution significantly.

### 2.2.1.2 AI-enhanced inhibitor deposition prediction

We adopt the neural network model shown in Figure 2.5 for inhibitor deposition prediction. During the forward process, the input data is fed through a Fourier layer to identify modal information, which is followed by an encoder structure that can transfer inputs into a  $z$ -length latent space, where  $z$  is equal to the number of deposition observation points. In this study, we generate 600 samples for model training and 50 samples for testing. Each sample contains the input ( $2 \times 99 \times 49$ ) with velocity fields in two directions and the output ( $2 \times 50$ ).

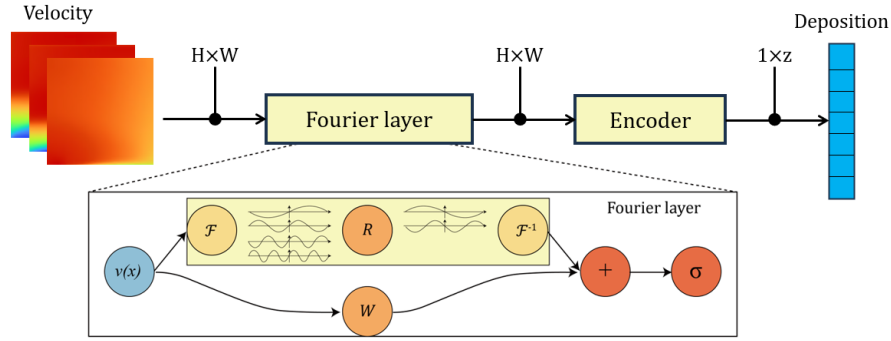


Figure 2.5: Neural network model for inhibitor deposition prediction.

To more clearly estimate the reliability of predictions, Bayesian uncertainty quantification is incorporated into all three frameworks, focusing on aleatoric uncertainty (AU). This type of uncertainty accounts for inherent noise and measurement inaccuracies in the data. The loss function used to model AU is as follows:

$$Loss = \frac{1}{N} \sum_{i=1}^N \left[ \frac{1}{2} \exp(-\sigma) \|y_i - \bar{x}\|^2 + \frac{1}{2} \sigma \right] \quad (2.1)$$

where  $N$  is the number of samples;  $y_i$  represents the ground truth values for the  $i$ -th sample;  $\bar{x}$  is the mean value of the predictions for the  $i$ -th sample and obtained from one branch of the network;  $\sigma$  is the standard deviation of the predictions, obtained from the second branch of the network. Figure 2.6 depicts the similarity between mean prediction and true values during training epochs. Several testing results with a 95% confidence interval (CI) are shown in Figure 2.7, in which the predicted values denote the mean prediction in Bayesian sampling. These samples are generated from randomly preset inlet velocities as illustrated in Figure 2.3, which leads to random velocity fields in the sampling region. It can be observed from the figure that the discrepancy between predicted and actual values is generally within 95% CI, indicating a strong relationship between local velocity and particle deposition. It is noted that some true values come from CFD simulations

show large fluctuations over spatial grid points, leading to larger uncertainty in some samples. This may be due to the inherent uncertainty of the atomizer, the calculation time step being too large, or insufficient training samples. Besides, predicted values can roughly follow the trend of true values, i.e., master modal features, which indicates the model’s ability to map velocity fields into particle deposition. The prediction uncertainty is potentially reduced by continuously improving the simulation setup to produce more high-quality samples.

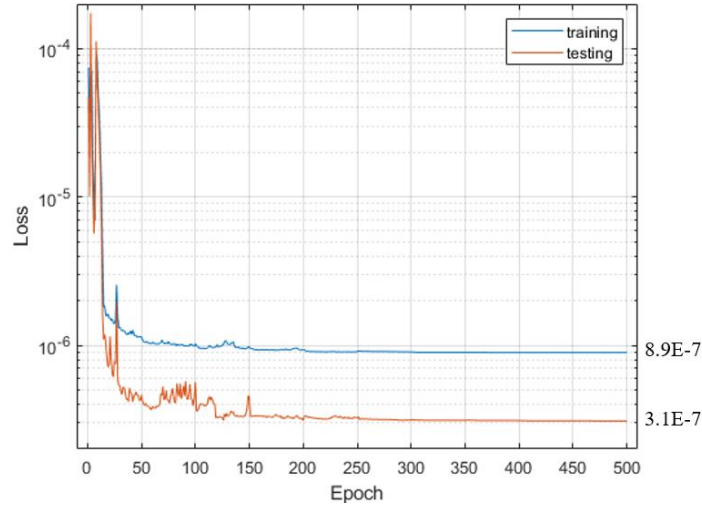


Figure 2.6: Similarity between mean prediction and true values during training epochs.

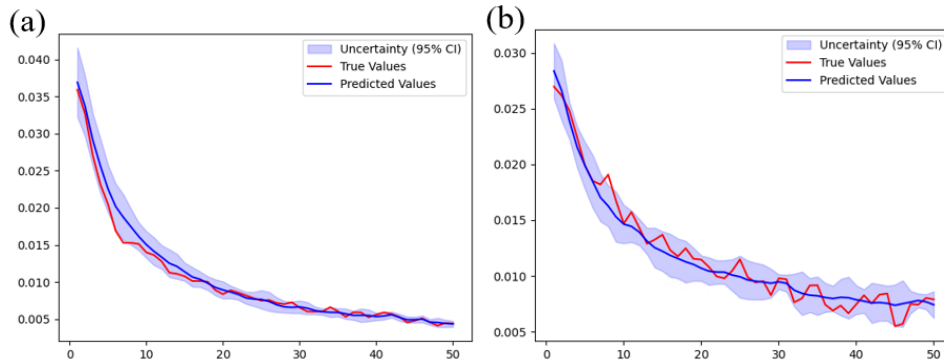


Figure 2.7: Two prediction results with uncertainty quantification under random velocity fields

a) random sample 1; b) random sample 2.

## 2.2.2 Probabilistic inhibitor degradation analysis with uncertainty quantification

### 2.2.2.1 Mechanism of corrosion inhibitor degradation

The effectiveness loss of the corrosion inhibitor under operational conditions potentially leads to unexpected pipeline damage and economic losses [2-5]. Existing research reveals that noticeable inhibitor degradation occurs mainly via thermal and microbial mechanisms. Fytianos et al. investigated the thermal degradation caused by Monoethanolamine decomposition [6]. Although Monoethanolamine is widely used in CO<sub>2</sub> capture, gas purification, water treatment, and

cleaning processes, it is not typically found in gas pipelines. Moreover, the study examined inhibitor degradation at around 120°C—a temperature that does not reflect the actual conditions in gas pipelines—thus limiting the applicability of the results to such environments.

As for microbial factors, Arijit et al. [7] isolated a sulfate-reducing bacterium (*Klebsiella pneumoniae* IIP-C3) from wastewater pipelines and exposed mild steel coupons to this microorganism in an anaerobic environment at 30°C. The paper provided the recorded corrosion rate and inhibitor efficiency over 30, 60, and 90 days, as shown in Figure 2.8, where ZO, FV, CA, and AI denote different plant extracts involved in inhibitors. In this experiment, sulfate-reducing bacteria were added to all samples after forming the inhibitor protective film. The figures reveal that microbial activity leads to the formation of biofilms, which facilitate the conversion of inorganic sulfates into organic polysulfides that subsequently react with the metal surface to produce corrosive FeS products.

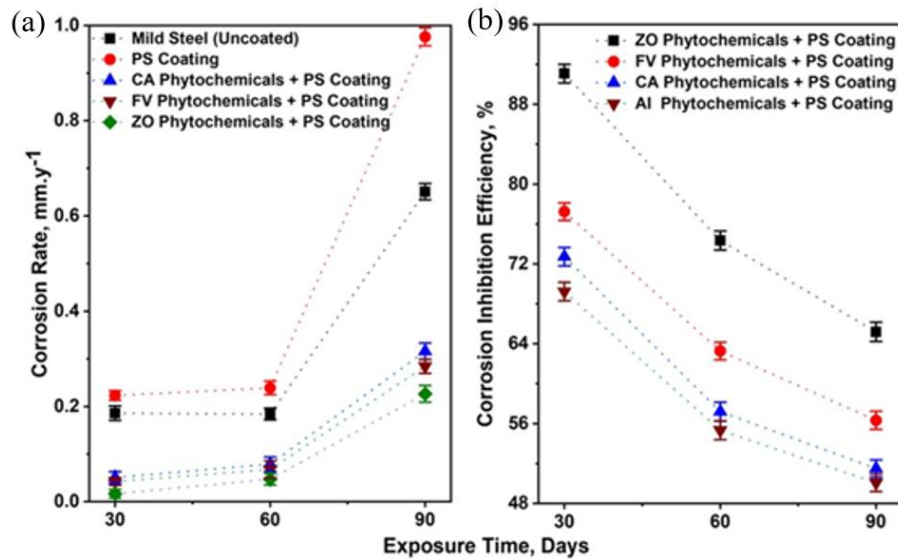


Figure 2.8: Corrosion rate and inhibitor efficiency of mild steel exposed to bacterial un-inoculated.

Aruliah et al. [8] specifically studied the effect of *Bacillus cereus* ACE4 on inhibitors' protective performance. A table provided in the paper emphasizes the comparison, as listed in Table 1. It is noted that groups 1 and 2 do not contain ACE4, and their corrosion rates increase to stable values. In contrast, groups 3 and 4 with ACE4 show not only larger corrosion rates than control groups but continuously increasing values along experimental periods. This reflects the harmfulness of microbial on protective film and provides support for the possibility of inhibitor degradation under operational conditions of the pipeline system.

Table 2.1 Corrosion rates of API 5LX with corrosion inhibitors in different systems

No.	System	Immersion period(h)	Corrosion rate (mm / year)
1	500ml diesel + 2% water + corrosion inhibitor I (10ppm)	80	0.003
		160	0.008
		240	0.01
2	500ml diesel + 2% water + corrosion Inhibitor II (10ppm)	80	0.019
		160	0.031
		240	0.031
3	500ml diesel + 2% water + ACE4 + corrosion inhibitor I (10ppm)	80	0.026
		160	0.027
		240	0.029
4	500ml diesel + 2% water + corrosion inhibitor II (10ppm) + ACE4	80	0.052
		160	0.064
		240	0.075

In addition to thermal and microbial mechanisms, chemical reactions and mechanical shock may also contribute to inhibitor degradation under operational conditions. For the former, the inhibitor may interact with chemical components in the transport media, potentially altering its molecular structure and diminishing its protective properties. As for mechanical shock, flow-propelled rigid particles or debris in the pipeline can physically scratch or erode the inhibitor's protective film, thereby exposing the underlying metal surface to corrosive agents. These mechanisms highlight the complexity of maintaining inhibitor integrity in dynamic pipeline environments.

### 2.2.2.2 Model development

In this section, we propose to establish a probabilistic model on inhibitor efficiency as the evaluation criterion. Previous sections illustrate the CFD simulation and deep learning techniques in predicting the inhibitor deposition. Although CFD allows us to efficiently obtain deposition conditions from many simulations, deposition does not directly reflect the protective performance of the inhibitor. Due to the molecular characteristics of the inhibitor, only a single monolayer can effectively adhere to the pipeline wall, meaning that deposition does not necessarily equate to being the actual protection film. At this point, we introduce inhibitor efficiency  $\phi_t$  to evaluate the protection performance [7]:

$$\phi_t \% = (C_0 - C_t)/C_0, \quad 0 < \phi < 100 \quad (2.2)$$

where  $C_0$  denotes the inherent corrosion rate in the absence of inhibitor;  $C_t$  and  $\phi_t$  are the corrosion rate and inhibitor efficiency at time  $t$ , respectively. It is noted that Eq. (2.2) is simplified that only captures the primary connection. However, it does not account for various influencing factors, such as the protection performance in covered areas with different media. Despite the simplification, the equation serves as a reasonable approximation for describing the overall trend of how efficiency influences the corrosion rate.

Combined with simulation results, initial efficiency  $\phi_0$  is determined by deposition  $D$  and is given by

$$\phi_0 = g(D) + \varepsilon_0 \quad (2.3)$$

where  $g(D)$  is an unknown monotonically increasing mapping that represents the influence of deposition on initial efficiency and  $\varepsilon_0$  is the noise depending on practical measurement conditions and the uncertainty of transfer between  $g(D)$  and  $\phi_0$ . It is no doubt that increasing deposition promotes the probability of inhibitor adhesion as well as efficiency and thus  $g(D)$  tends to be a monotonically increasing function. Inhibitor deposition is assumed to follow the normal distribution with the mean value  $\mu$  and the standard deviation  $\sigma$  as:

$$D \sim N(\mu_D, \sigma_D^2) \quad (2.4)$$

Based on the assumptions above, we construct a probabilistic model to describe the degradation of efficiency over time. Initial efficiency at  $t=0$  is given by

$$\phi_0 \sim N(g(D), \varepsilon_0^2) \quad (2.5)$$

The specific form of the function  $g(D)$  requires experimental quantification to establish the relationship between inhibitor deposition and the protective film coverage within a localized test area, or the evaluation of the corrosion rate along pipe segments where the inhibitor particles are evenly distributed. Despite a lack of systematic studies dedicated to validating the functional form of  $g(D)$ , the introduction of the probabilistic model will not be impaired, since there is existing inhibition efficiency data from the reference used for illustration in the next section.

To capture the smooth degradation of efficiency over time, we impose a parametric prior model expressed as:

$$\phi_t \sim N(f(t), \tau^2), \quad t = 2, 3, 4, \dots \quad (2.6)$$

where the model parameters in the function  $f(\cdot)$  are estimated through nonlinear least square regression, and their uncertainties are quantified using posterior sampling; the process noise  $\tau^2$  represents the variance of change between adjacent time points. The Monte Carlo sampling is performed to propagate uncertainty through time, allowing for a probabilistic forecast of future efficiency values. The identified model parameters can be gradually updated with new inspection data that keeps improving the prediction performance of the probabilistic model.

At each time  $t$ , the inspection model is expressed as

$$\phi_{obs,t} \sim N(\phi_t, \varepsilon^2) \quad (2.7)$$

With the  $\varepsilon^2 \sim N(0, \sigma^2)$  representing the variance of inspection noise. This model, which does not require specifying a deterministic function for the efficiency decay over time, leverages the temporal smoothness captured by the prior while incorporating the effect of the deposition on initial efficiency.

### 2.2.2.3 Verification and validation

#### 2.2.2.3.1 Validation based on existing experimental data

This section aims to illustrate the applicability of the proposed probabilistic model based on the inhibition efficiency data under microbial corrosion presented in Figure 8 of Ref. [7]. The inhibition efficiency data in Ref. [7] were obtained under wastewater pipeline conditions. We did not find representative experimental data in natural gas pipelines for inhibitor degradation testing. We use the collected for demonstration purposes. In natural gas pipelines, it is possible for liquid accumulation to occur at low points or in areas with special geometric pipeline layouts, such as elbows due to obstacles. These localized environments may resemble the conditions studied in the reference, such as the presence of water phases and corrosive species. Therefore, while the operating environments differ in general, we use this data to study scenarios where similar corrosion mechanisms could occur due to water accumulation. The data is re-depicted in Figure 2.9, in which we can observe three samples describing efficiency degradation. The reference also shows that the noise for each inspection is 0.89, i.e.,  $\sigma = 0.89$  in Eq. (2.7). These samples have different initial conditions at the time 30 that is regarded due to the uncertainty of deposition. Nevertheless, all samples follow similar degradation trends, and based on that, we consider the following degradation function:

$$\phi_t = a\phi_{t-1} + b \quad (2.8)$$

Unlike that  $\phi_0$  depends on  $g(D)$  according to Eq. (2.6), we establish the normal distribution for  $\phi_0$  based on available samples, i.e.,  $\phi_0 \sim N(\mu_0, \tau_0^2)$ .

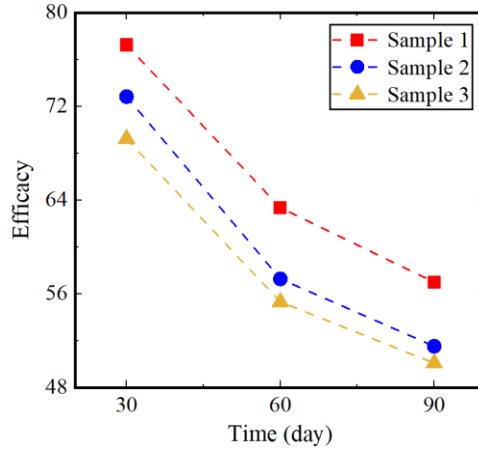


Figure 2.9: Data of 3 samples used to build the probabilistic model.

In practical applications, the efficiency degradation model can be gradually updated by obtaining inspection data. Considering only three time points are provided, we adopt two stages to improve the model's performance in uncertainty quantification. In Stage 1, the model is first trained using only the inspections  $\phi_0$  and  $\phi_1$  (i.e., efficiency at time 30 and 60). As additional efficiency  $\phi_2$  becomes available in Stage 2, the model is refitted to refine the estimated parameters  $a$  and  $b$ , thereby improving prediction accuracy and uncertainty quantification.

Stage 1 where only  $\phi_0$  and  $\phi_1$  are available, is first illustrated. The nonlinear least-squares regression is applied to minimize the squared difference between the observed value  $\phi_{1,obs}$  and the model-predicted value  $a\phi_{0,obs} + b$ . Due to the lack of data out of time 60, the uncertainty of  $\phi_2$  and  $\phi_3$  based on the current degradation model mainly comes from the uncertainty of model parameters and the inspection noise. To achieve this, we construct an approximate distribution using a local Gaussian approximation around the least-squares solution, in which the mean estimates are denoted by  $[\hat{a}, \hat{b}]$ , and the covariance matrix is computed as:

$$\Sigma_{[a,b]} = s^2 (J^T J)^{-1} \quad (2.9)$$

$$s^2 = \frac{1}{n-p} \sum_{i=1}^n r_i^2 \quad (2.10)$$

$$r_i = \phi_{t,obs}^{(i)} - (a\phi_{t-1,obs}^{(i)} + b) \quad (2.11)$$

$$J = \begin{bmatrix} \partial r_1 / \partial a & \partial r_1 / \partial b \\ \vdots & \vdots \\ \partial r_n / \partial a & \partial r_n / \partial b \end{bmatrix} = \begin{bmatrix} -\phi_{t-1}^{(1)} & -1 \\ \vdots & \vdots \\ -\phi_{t-1}^{(n)} & -1 \end{bmatrix}$$

(2.11)

where  $r_i$  denotes the residual at the  $i$ -th inspection and  $s^2$  is the residual variance;  $n=6$  is the number of data points and  $p=2$  is the number of parameters;  $J$  is the Jacobian matrix consisting of the partial derivatives of the residuals with respect to each parameter.

After obtaining parameter distribution  $\Sigma_{[a,b]}$ , we proceed to generate probabilistic forecasts for the future efficiency  $\phi_2$  and  $\phi_3$ . This is achieved via Monte Carlo sampling and recursive simulation. In the  $k$ -th sampling step, a set of parameters  $[a^k, b^k]$  is sampled from the multivariate distribution  $N([\hat{a}, \hat{b}], \Sigma_{[a,b]})$ . Then, the degradation trajectory starting from  $\phi_0$  sampled in  $N(\mu_0, \tau_0^2)$  is simulated with  $\phi_t^k = a^k \phi_{t-1}^k + b^k + \varepsilon$ , where  $\varepsilon$  is sampled from  $N(0, 0.89^2)$ . The maximum number of  $k$  is set to 10000 for the Monte Carlo simulation to yield satisfactory approximation of the predictive distribution, which is based on the available data points only at time 30 and 60.

Once the additional inspection  $\phi_2$  becomes available in Stage 2, the model is re-estimated using both inspection pairs  $(\phi_0, \phi_1)$  and  $(\phi_1, \phi_2)$ . This expanded dataset provides more information to constrain the model parameters. Following the same procedure, a new Gaussian approximation of the parameter distribution is constructed based on minimizing the residual over 3 points. A new set of Monte Carlo samples is drawn from the updated posterior, and recursive simulation is repeated to generate the predicted distributions of future efficiency  $\phi_2$  and  $\phi_3$  once again.

Depicting in Figure 2.10, a direct comparison of the predictive distributions between Stage 1 and Stage 2 reveals the impact of incorporating additional inspections on uncertainty quantification. Stage 1 and Stage 2 adopt the same initial samples, and thus, the same distributions are achieved  $\phi_0$ . Besides, all the predicted densities shrink and that of  $\phi_2$  shift toward the true values as the model progresses from Stage 1 to Stage 2. In Stage 1, where only  $\phi_0$  and  $\phi_1$  are

available, the parameter posterior is wide, resulting in a broad distribution for  $\phi_2$  and especially  $\phi_3$ . Figure 2.11 gives a temporal view of inhibitor efficiency degradation with uncertainty bounds in Stage 2. In contrast, it introduces new information of  $\phi_2$  leads to a significantly narrower predictive distribution. This effect is particularly evident on the longer horizon  $\phi_3$ , where the uncertainty accumulated from recursive simulation is more pronounced in Stage 1 than in Stage 2. The above comparison highlights that the inspection data updating process with newly acquired inspection contributes to improving the accuracy and reliability of parameter estimation.

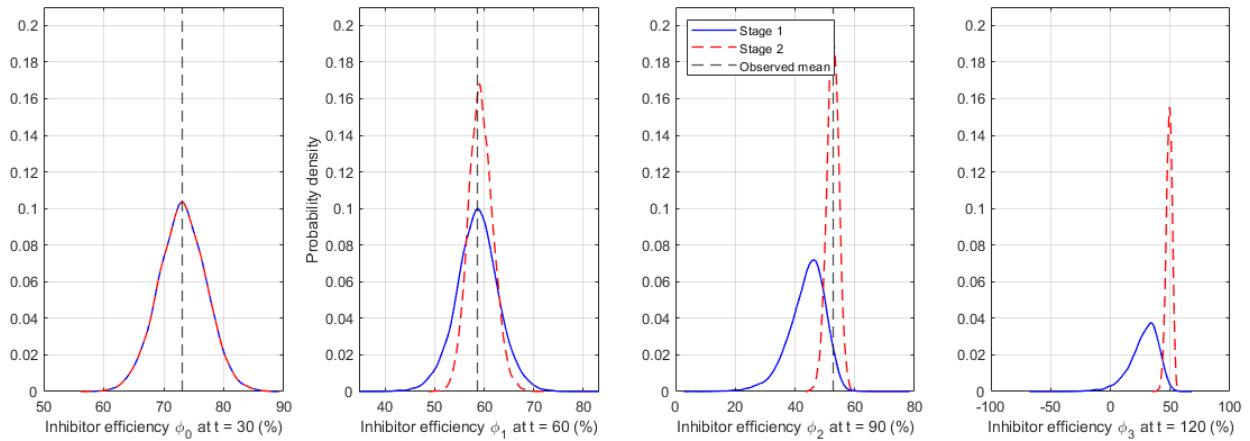


Figure 2.10: Comparison of efficiency degradation estimation between Stage 1 and Stage 2.

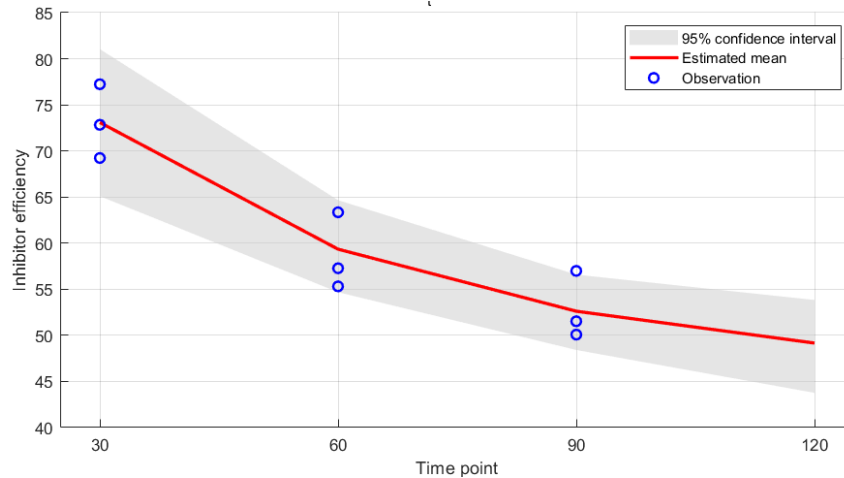


Figure 2.11: Inhibitor efficiency degradation with uncertainty bounds in Stage 2.

### 2.2.2.3.2 Verification based on synthetic numerical data

A numerical simulation is performed to further verify the effectiveness of the uncertainty analysis method with inspection data updating. In this case, the initial inhibitor efficiency is generated by  $\phi_0 = 100[1 - \exp(-230D)]$ , where  $D \sim N(0.01, 0.0015^2)$ . The efficiency over time is determined by  $\phi_t = \phi_0 \exp(-k_1 t + k_2) + \varepsilon$ , where  $k_1 \sim N(0.02, 0.002^2)$ ,  $k_2 \sim N(-0.001, 0.0001^2)$ ,  $\varepsilon \sim N(0, 1^2)$ . We still adopt the probabilistic inhibitor degradation model

$\phi_t = a\phi_{t-1} + b$ , and perform similar stages described in Section 2.2.2.3.1 with 20 inspection time points in 10 samples. Figure 2.12 depicts the inhibitor efficiency degradation with uncertainty bounds in the final time stage, i.e., the 20<sup>th</sup> time point, in which the 30<sup>th</sup> time point is predicted. The figure indicates that the model not only captures the overall degradation trend but also effectively reflects the uncertainty inherent in the degradation process. The ability of the model to account for observed variability suggests that its predictions are reliable, thereby providing a credible basis for forecasting future inhibitor performance under similar conditions.

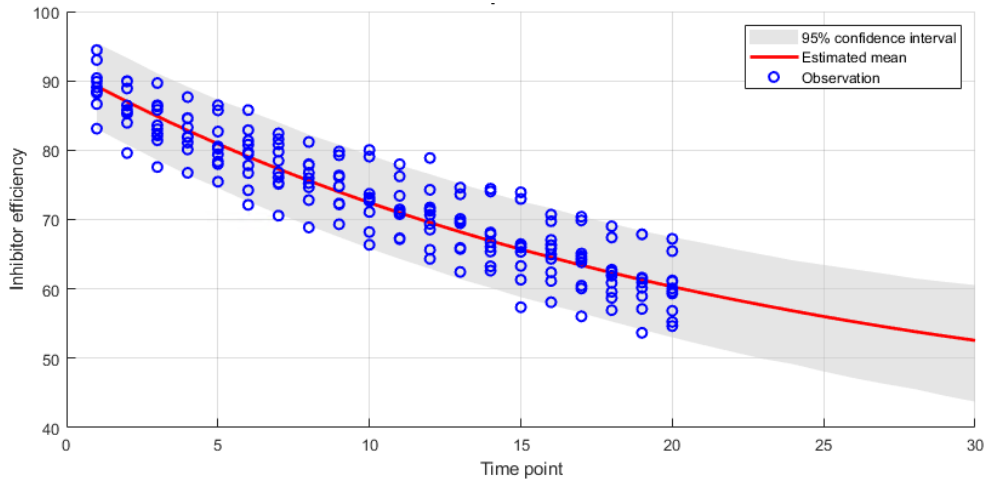


Figure 2.12: Inhibitor efficiency degradation with uncertainty bounds in the final time stage.

## 2.3 Future research

The current study has successfully established a prediction model for inhibitor deposition across various pipe geometries, where the results from the AI-enhanced CFD simulations are subsequently integrated into a probabilistic model that quantifies the uncertainty in inhibitor efficiency, a key index for evaluating the reliability of the inhibitor film. However, despite these advancements, there are notable limitations in the current approach that warrant further discussion. First, the AI-enhanced deposition prediction approach only considers straight pipe simulation, which is hard to apply in the pipeline system with changing geometries. The current well-trained neural network model does not include the coordinated information of the pipe wall and velocity field. To address this issue, a future study aims to design an adaptive mapping module involved in the model that is able to transfer the flow data under different geometries into the same latent space for further usage.

Another major shortcoming is the lack of a clearly defined relationship between initial inhibitor efficiency and deposition. At present, the model proposes that inhibitor efficiency in practical applications can be indirectly inferred from the measured corrosion rate, thereby enabling a fitting of a function that relates to deposition. Nevertheless, the formulation of the relationship between the corrosion rate and inhibitor efficiency presented herein is rather simplified and does not fully account for the complexities inherent in real-world operating environments. Factors such as dynamic flow conditions, variable chemical compositions, and other operational parameters that

may influence both the deposition process and the performance of the inhibitor film are not comprehensively addressed.

Future experimental work is essential to bridge this gap, as it would allow for a more robust understanding of the interplay between deposition and inhibitor effectiveness. To this end, beginning with Q7, our forthcoming research phase titled “Inhibitor Measurements and Data Analytics” will be undertaken. This phase will leverage state-of-the-art optical non-destructive testing methods and AI-based stereo vision techniques to accurately assess various properties of the inhibitor film, including its thickness and coverage. The integration of these advanced measurement technologies is expected to provide richer, more detailed data that can be used to refine the reliability model, thereby improving the linkage between CFD predictions and the practical implementation of inhibitor injection strategies.

With the availability of richer measurement data, future work will also focus on building a Bayesian risk assessment model that allows for more efficient and adaptive evaluation of inhibitor performance under uncertainty. This model will incorporate prior knowledge from CFD-based deposition predictions and update reliability estimates using real-time or inspection-based observational data through Bayesian inference. The framework can dynamically adjust to new evidence, quantify predictive uncertainty, and support decision-making for optimal injection strategies by modeling the inhibitor efficiency as a stochastic process with hierarchical priors. The probabilistic outputs of the Bayesian model will enable risk-informed maintenance scheduling and localized corrosion prevention in complex pipeline systems.

In summary, while our current model lays an important foundation, further experimental validation and the incorporation of additional environmental complexities will be crucial to fully realize and enhance the predictive capability and reliability of inhibitor deposition models in real-world applications.

## References

1. Al-Moubaraki, A. H., and I. B. Obot, Top of the line corrosion: causes, mechanisms, and mitigation using corrosion inhibitors. *Arabian Journal of Chemistry*, 2021. 14(5): p. 103116.
2. Aslam R, Mobin M, Zehra S, et al. A comprehensive review of corrosion inhibitors employed to mitigate stainless steel corrosion in different environments[J]. *Journal of Molecular Liquids*, 2022, 364: 119992.
3. Shwetha K M, Praveen B M, Devendra B K. A review on corrosion inhibitors: types, mechanisms, electrochemical analysis, corrosion rate and efficiency of corrosion inhibitors on mild steel in an acidic environment[J]. *Results in Surfaces and Interfaces*, 2024: 100258.
4. Berrissoul A, Ouarhach A, Benhiba F, et al. Exploitation of a new green inhibitor against mild steel corrosion in HCl: Experimental, DFT and MD simulation approach[J]. *Journal of Molecular Liquids*, 2022, 349: 118102.
5. Fytianos G, Vevelstad S J, Knuutila H K. Degradation and corrosion inhibitors for MEA-based CO<sub>2</sub> capture plants[J]. *International Journal of Greenhouse Gas Control*, 2016, 50: 240-247.
6. Fytianos G, Vevelstad S J, Knuutila H K. Degradation and corrosion inhibitors for MEA-based CO<sub>2</sub> capture plants[J]. *International Journal of Greenhouse Gas Control*, 2016, 50: 240-247.
7. Jana A, Sarkar T K, Chouhan A, et al. Microbiologically influenced corrosion of wastewater pipeline and its mitigation by phytochemicals: Mechanistic evaluation based on spectroscopic, microscopic and theoretical analyses[J]. *Journal of Molecular Liquids*, 2022, 364: 119960.
8. Rajasekar A, Maruthamuthu S, Palaniswamy N, et al. Biodegradation of corrosion inhibitors and their influence on petroleum product pipeline[J]. *Microbiological Research*, 2007, 162(4): 355-368.
9. Jayaweera C D, Fernandes del Pozo D, Hitsov I P, et al. Assessing the feasibility of using a data-driven corrosion rate model for optimizing dosages of corrosion inhibitors[J]. *npj Materials Degradation*, 2024, 8(1): 127.

**Appendix 3**  
**Presentation File for Quarterly TAP Meeting**